ISPRS Journal of Photogrammetry and Remote Sensing 207 (2024) 264–281

Contents lists available at ScienceDirect

ISPRS Journal of Photogrammetry and Remote Sensing

journal homepage: www.elsevier.com/locate/isprsjprs

Automatic differentiation of *Eucalyptus* species through Sentinel-2 images, Worldview-3 images and LiDAR data

L. Alonso [a,b,*], A. Rodríguez-Dorna [a,b], J. Picos [a], F. Costas [a], J. Armesto [a,b]

[a] Universidade de Vigo, Escola de Enxeñaría Forestal, 36005 Pontevedra, Spain
[b] CINTECX, Universidade de Vigo, Grupo Xestión Segura e Sostible de Recursos Minerais (XESSMin), 36310 Vigo, Spain

ARTICLE INFO

Keywords:
Forest
Eucalyptus
LiDAR
Sentinel-2
Worldview
Textures

ABSTRACT

Eucalyptus constitutes one of the most common tree genera used in forest plantations worldwide. In Europe, *Eucalyptus* trees are especially common in the Northwest of the Iberian Peninsula, *E. nitens* and *E. globulus* being the most commonly cultivated species. Each species presents particularities that lend to different exploitation strategies and industrial usages. Therefore, updated knowledge about the abundance and spatial distribution of the different species is important for forest planning. This is a special challenge for areas where forest land is highly fragmented. Remote sensing has been used to efficiently monitor the distribution of the *Eucalyptus* genera, however little research has been able to map specific *Eucalyptus* species. This study evaluates the efficiency of Sentinel-2 data, Worldview-3 images, and Airborne LiDAR data in the differentiation of *E. nitens* and *E. globulus*. Supervised classifications were performed using neural networks for these data sets both individually and in combination. The highest accuracies were obtained when using Sentinel-2 data in combination with LiDAR point clouds and when using Sentinel-2 data in a multitemporal approach. The best time of year to differentiate between the two species is during the emergence of spring shoots. Worldview-3 images have a moderate capacity to differentiate between the two species, although this is increased when textural metrics are included. This study can serve as the basis for generating *Eucalyptus* species distribution maps, which will allow for improved forest management and planning.

1. Introduction

Knowledge about the distribution of tree species is essential for sustainable forest management and planning (Santopuoli et al., 2021; Barrio-Anta et al., 2021). One of the tree genera that is essential to monitor is *Eucalyptus,* since it plays a key role in the forest sector worldwide. *Eucalyptus* trees are planted all over the world, from the tropics (Messier et al., 2021) to temperate forests (Tomé et al., 2021), and they have multiple industrial usages, such as in the pulp and paper industry and in the bioenergy industries as well as for producing different engineered-wood products (Tomé et al., 2021). According to Harwood (2011), of the 700 different naturally-occurring *Eucalyptus* species (Coppen, 2002), the most cultivated *Eucalyptus* species are *E. camaldulensis*, *E. grandis*, *E. tereticornis*, *E. globulus*, *E. nitens*, *E. urophylla*, *E. saligna*, *E. dunnii*, *E. pellita* and some of their hybrids. Different species lend themselves to different applications and industrial usages (Ramnath et al., 2018; Acuña et al., 2020; Domingues et al., 2011; Seng Hua et al., 2022; Pérez-Cruzado et al., 2011). Additionally, different species have different characteristics that condition their growth in different environments (Ngugi et al., 2015; Pérez-Cruzado et al., 2011). Furthermore, it has been observed that certain *Eucalyptus* species in specific environments and management conditions have the potential to become invasive and may have multiple impacts on the environment, thus compromising the conservation of natural forests (Forsyth et al., 2004; Calviño-Cancela and van Etten, 2018; MITECO, 2017; Tomé et al., 2021). Therefore, being able to effectively map different *Eucalyptus* species is essential for forest and nature conservation stakeholders.

In Europe, *Eucalyptus* is most commonly cultivated in Northwest of the Iberian Peninsula (Brus et al., 2011). In Portugal around 26% of the continental forest area is covered by *Eucalyptus* (ICNF, 2015), and the most recent Spanish NFI (National Forest Inventory) reported that in Galicia (A region in northwestern Spain), approximately 20% of the total forested area is covered by *Eucalyptus* as well (MITECO, 2011a). Therefore, *Eucalyptus* plantations represent an important commodity for the forest industries in these regions (Xunta de Galicia, 2023).

* Corresponding author at: Universidade de Vigo, Escola de Enxeñaría Forestal, 36005 Pontevedra, Spain.
E-mail address: laura.alonso.martinez@uvigo.es (L. Alonso).

https://doi.org/10.1016/j.isprsjprs.2023.12.010
Received 5 May 2023; Received in revised form 18 December 2023; Accepted 25 December 2023
Available online 29 December 2023

Additionally, concerns have arisen among nature conservation stakeholders about the distribution and abundance of these plantations (Pérez-Cruzado et al., 2011; MITECO, 2017; Calviño-Cancela and van Etten, 2018; Tomé et al., 2021). In these regions, the most commonly cultivated species are *Eucalyptus globulus* and *Eucalyptus nitens* (MITECO, 2011a). These two species present particularities that imply different growth strategies and lend themselves to different applications. For example, it has been reported that they present differences in their growth rates and frost tolerances (Pérez-Cruzado et al., 2011; Close et al., 2000; Davidson et al., 2004). Similarly, their responses to growth stress, wounds, pruning and pathogens are also different (Beadle et al., 2001; Deflorio et al., 2007; Wiseman et al., 2009, Gonçalves et al., 2019; Smith et al. 2007). Disparities have also been identified in the carbon litter accumulation of each species (Pérez-Cruzado et al., 2011). Regarding their applications, *E. globulus* has proven to be more relevant for the pulp industry (Antes & Joutsimo, 2015; Pérez et al., 2006; Pérez-Cruzado et al., 2011) because of its better pulp yield and quality (Kibblewhite et al 2000). Despite these differences, the distribution of the two species in Europe has hardly been assessed. In Spain, the most recent data available on the distribution of *Eucalyptus* species dates from 2011 (MITECO, 2011a). Considering that the rotation cycles for both species are between 12 and 15 years (Tolosana et al., 2017; Arenas et al., 2019), and the perceived recent trend in forest owners replacing E. globulus for E. nitens, this distribution data might be outdated. In the case of Portugal, the Portuguese NFI does not disaggregate the different *Eucalyptus* species (ICNF, 2015). An additional drawback is that this information is currently acquired through field work, making it difficult to update more frequently or increase the level of detail. It is therefore beneficial to develop new methods that yield updated information about the distribution of *Eucalyptus* species in these regions.

Remote sensing has been widely used to monitor *Eucalyptus* distribution around the globe (Sibanda et al., 2021; da Costa et al., 2022; Deng et al., 2020) and also in the Northwest of the Iberian Peninsula in particular (Forstmaier et al., 2020; Alonso et al., 2021a; Alonso et al., 2021b; Oliveira et al., 2021). The most commonly implemented remote sensing tool used to identify *Eucalyptus* plantations and forests is passive remote sensing (this is the case in the studies mentioned above), however some studies have also incorporated LiDAR data (Novo-Gomez et al., 2022; Wu and Zhang, 2020). Despite the great amount of research focused on identifying *Eucalyptus* stands, there has thus far been little research aimed at distinguishing between *Eucalyptus* species. In the case of passive remote sensing, the distribution of *Eucalyptus* species has been studied using hyperspectral images and very high-resolution multispectral images. For example, the Peerbhay et al. (2013) study compiles the results of several studies on the ability of hyperspectral imagery to distinguish between *Eucalyptus* species. Many of these studies highlighted the difficulty of this task, especially when dealing with certain combinations of species. However, the Shang and Chisholm (2014) study demonstrates the ability of hyperspectral data to differentiate between *Eucalyptus* species in an Australian native forest. Peerbhay et al. (2013) also assess the possibility of using hyperspectral imagery to distinguishing between the *Eucalyptus* species that commonly grow in South Africa, showing that the most important wavebands for this task are located in the visible spectrum, and providing evidence that attests to the capability of very-high resolution multispectral data. However, few studies have addressed the possibility of using very-high resolution multispectral images for distinguishing between *Euclayptus* species. One example is the subsequent study of Peerbhay et al. (2014) that obtained user's and producer's accuracies of between 80 and 100 percent for *E. grandis*, *E. nitens* and *E. smithii* using Worldview-2 in South Africa. In the same sense, Alonso et al. (2021b) have explored the capacity of Worldview-3 to distinguish between *E. globulus* and *E. nitens* in a pilot area in Spain, obtaining lower user's and producer's accuracies (of between 45% and 84%) for this particular combination of *Eucalyptus* species. They remark that further research in different locations and using different remote sensing data may be necessary to improve accuracy results. One option could be to incorporate LiDAR data, as was done by Verma et al. (2019), who explored the capacity of LiDAR data and multispectral images to classify five different species of *Eucalyptus* in a native forest and found that the most accurate results were obtained when using LiDAR and multispectral images combined. A similar conclusion was reached in the study of Yadav et al. (2021), which also highlight the advantages of including LiDAR data in the classification of *Eucalyptus* species in native forests.

Given the importance of mapping the distribution of different *Eucalyptus* species, this study evaluates the utility of different remote sensing data sources for mapping *E. globulus* and *E. nitens*. The sensors analyzed were very high-resolution Worldview-3 images with spectral and textural metrics, open-access Sentinel-2 images, and airborne LiDAR data. The study area is located on the Iberian Peninsula, in a region with one of the highest abundances of these two *Eucalyptus* species in all of Europe.

2. Case study

2.1. Study area

The study was conducted in the region of Galicia, in the northwest of Spain. The study area, which can be seen in Fig. 1C on dark green, was an area where very high-resolution multispectral imagery and recent LiDAR data were available. It covers a total area of 3611 km^2. Fig. 1C shows the distribution of *Eucalyptus* in Galicia according to the 2020 Sentinel-2 forest-oriented land cover map of Galicia (Alonso et al., 2022). On Fig. 1B is possible to see that currently *Eucalyptus* is mostly present on coastal areas. According to the latest forest inventory *E. globulus* and *E. nitens* are present in Galicia (Miteco, 2011b).

2.2. Species studied

Eucalyptus tree plantations began to appear in Galicia in the middle of the 19th century when an afforestation process began in the region. *Eucalyptus globulus* was the first species to be planted (Barrio-Anta et al., 2021). *Eucalyptus nitens* was not introduced in this afforestation process and has only appeared in the last two decades; plantations of this species started to appear due to its greater resistance to *E. globulus* pests and its greater frost tolerance (Neilan and Thompson, 2008, Aguín et al., 2013; Ayuga-Téllez et al., 2022; Tomé et al., 2021) Therefore, the most abundant species, according to the latest records, is *E. globulus* (Miteco, 2011b). *Eucalyptus* plantations in this region are mostly owned by small non-industrial private owners (Tomé et al., 2021). Therefore, few management practices are applied (Tomé et al., 2021, González-Gómez et al., 2011). There is also evidence, especially in the case of *E. globulus*, of unmanaged and abandoned plantations due to recurring wildfires or to the plantations being in unsuitable areas (Tomé et al., 2021). All of these factors may lead to greater heterogeneity in terms of age, height, diameter and structure of *E. globulus* stands in comparison with *E. nitens* stands. Plantation densities for both species in Galicia are the same, they are usually planted using a range of 1000–1600 trees per hectare (DOG, 2021).

At a glance, the two species are similar. The main characteristics that help to differentiate between them are their flowers and fruit (Orwa et al. 2009, López, 2002). However, other characteristics have been described that can help to differentiate between the two when these elements are not present. *E. globulus* is prone to coppice regeneration while this hardly ever occurs in *E. nitens* stands (Gutiérrez, 1976; Neilan and Thompson, 2008). Additionally, persistence of dead branches is more typical of *E. nitens* stands (Pinkard, 2002; Pérez-Cruzado and Rodríguez-Soalleiro, 2011). In addition, field practice has identified different coloration during peak budding as a distinguishing characteristic. Thus, as stated by the BASOA Foundation (2017), spring shoots in *E. globulus* tend to exhibit a greenish coloration, while those of *E. nitens* tend to show reddish tones. Understory species that tend to be associated

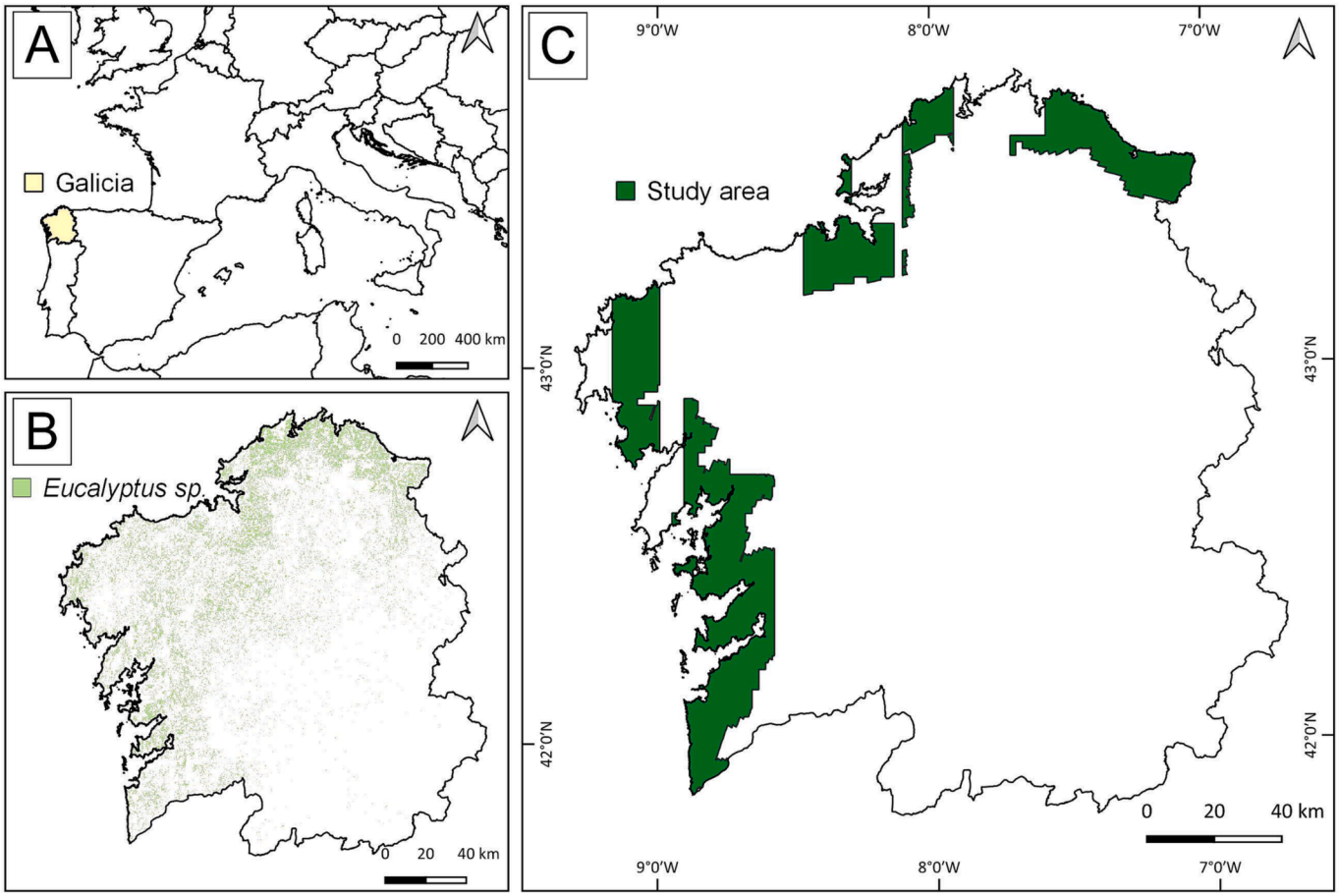

Fig. 1. Study area. C: representation of the Eucalyptus distribution which corresponds to the land cover map by Alonso et al. (2022).

to both *Eucalyptus* species are the same. Images of typical stands of each of the two species are shown in Fig. 2, both images being captured in planted stands with a high-growth age and heights of greater than 15 m.

Few studies about the phenological behaviors of the *Eucalyptus* species under study have been accomplished. Some studies on this topic have been accomplished in Tasmania and South America. According to

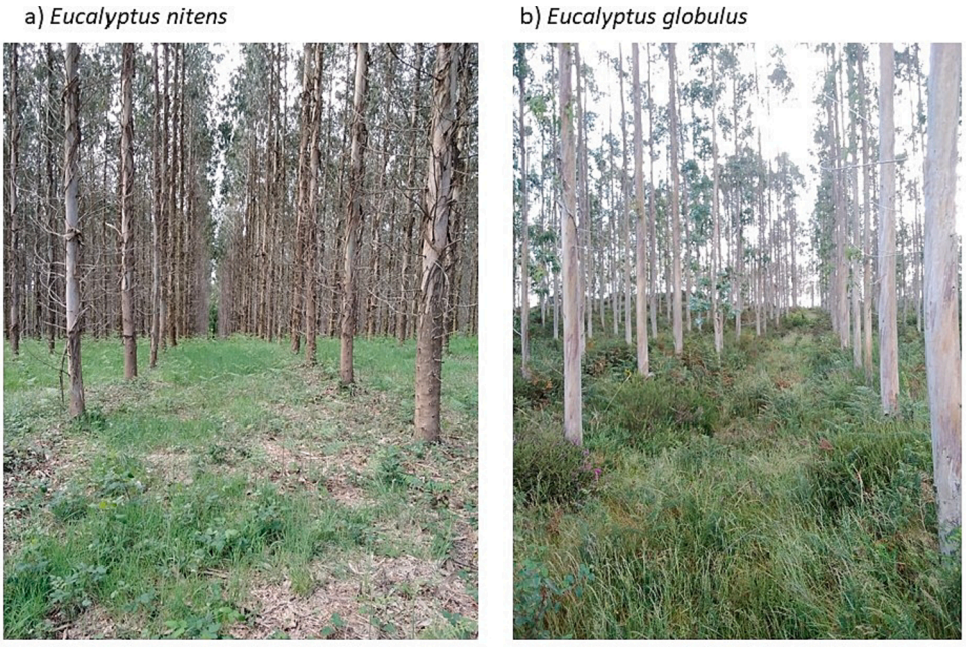

Fig. 2. Examples of stands of the two *Eucalyptus* species present in the study area. Left *E. nitens* and right *E. globulus*. Both images were captured in planted stands with a high-growth age and heights greater than 15 m.

Downes et al. (1999) study performed over *Eucalyptus* plantations in Tasmania, *E. nitens* tended to have longer increment phases in spring and autumn, and faster phase rates in autumn than *E. globulus*. Battaglia et al. (1996) developed their study over Tasmanian plantations and concluded that the photosynthetic temperature response curve of *E. nitens* may be wider compared to *E. globulus*. For a different geographic region (Chile) Watt et al. (2014) stated that the air temperature modifier for *E. nitens* for a process-based model exhibited dual peaks during late spring/early summer and then again in early autumn when air temperatures were closest to the optimum air temperature for growing.

According to the own experience of the authors and their knowledge of the study area, the spring months (March to May) are associated with the main peak budding for both species in the study area, although buds can occur during the whole year. The flowering in *Eucalyptus nitens* is infrequent and light (Moncur and Hasan, 1994). The flowering of *Eucalytpus globulus* takes places in Galicia from autumn to early summer according to Calviño-Cancela and Rubido-Bará (2013).

3. Materials

3.1. Worldview-3 images

Worldview-3 is a commercial satellite launched in 2014. One of the products acquired from this instrument is comprised of eight multispectral bands each with a spatial resolution of 1.2 m. Detailed information about the spectral ranges is presented in Table 1.

The WorldView-3 images that were used in this study were gathered in two blocks acquired at different dates. The first block was acquired between May and June of 2021 and a second block was acquired between August and October of 2021. It was not possible to acquire all the study area at the same date due to the cloud cover, according to the image provider. The specific date of the images and the acquisition parameters are shown in Table 2. Varying dates involve different sun elevation angles, and consequently different projected shadows; but also they usually involve different phenological stages and subsequent variations in the digital values of land covers. The images of these two blocks also differ in the preprocessing procedure. The digital values of the images are the result of applying atmospheric, radiometric and geometric corrections to the original scenes. According to the image provider, the algorithms that were used to correct the images were different for the two blocks. As a result, the digital values of analogous land covers are significantly different in both blocks. Because of these differences the two blocks were processed separately.

3.2. Sentinel-2 images

Images of the constellation of satellites Sentinel-2 were used on this study. These images have information on 13 spectral bands with a spatial resolution ranging from 10 m to 60 m, depending on the band (ESA, 2015). The specifications of the spectral bands are shown in Table 3.

The Sentinel-2 mission has a high revisit time: 10 days at the equator with one satellite, and 5 days with 2 satellites under cloud-free conditions which results in 2–3 days at mid-latitudes. One image per month was used in this study to cover the different phenological stages of *Eucalyptus*. For the study area, the least cloudy image available from each month was selected. Images were downloaded from the Copernicus Open Hub (ESA, n.d.). The product downloaded was the Level 2A since it has geometric, radiometric, and atmospheric corrections (ESA, n.d.b). The Sentinel-2 bands used in this study were the 10 m and 20 m ones. Appendix A presents the dates of the images used for each month and Sentinel-2 tile.

Table 1
Spectral characteristics of Worldview-3 images.

Band name	Wavelength ranges (nm)
Coastal Blue	400–450
Blue	450–510
Green	510–580
Yellow	585–625
Red	630–690
Red Edge	705–745
NIR-1	770–895
NIR-2	860–1040

Table 2
Acquisition dates and acquisition parameters of Worldview-3 images.

Block	DATE	Sensor azimuth	Sun azimuth	Sun elevation
1	2021-05-03	53	148	60
1	2021-05-03	100	148	60
1	2021-05-03	98	148	60
1	2021-05-29	245	148	67
1	2021-05-29	313	151	66
1	2021-05-29	291	149	67
1	2021-06-04	355	145	67
1	2021-07-18	343	144	64
2	2021-08-25	351	154	55
2	2021-08-25	242	154	55
2	2021-08-25	349	153	55
2	2021-10-07	72	161	39
2	2021-10-14	358	166	37
2	2021-10-14	193	165	37
2	2021-10-26	73	164	33
2	2021-10-26	73	164	33

Table 3
Sentinel-2 bands.

Band name	Central wavelength (nm)	Resolution (m)
B01-Coastal aerosol	443	60
B02-Blue	490	10
B03-Green	560	10
B04-Red	665	10
B05-Red Edge 1	705	20
B06-Red Edge 2	740	20
B07-Red Edge 3	783	20
B08-NIR 1	842	10
B8A-NIR 2	865	20
B09-Water vapor	945	60
B10-SWIR - Cirrus	1375	60
B11-SWIR 1	1610	20
B12-SWIR 2	2190	20

3.3. LiDAR data

LiDAR data for the whole study area was obtained using an airborne laser scanner (ALS). All the LiDAR data was acquired during November of 2019. The LiDAR acquisition density was >3 points/m^2. This data was provided by the Administration of Rural Areas of the Government of Galicia.

4. Methodology

4.1. Reference data collection

Reference data for the two species was obtained through field work in the year 2021. In order to define enough reference data for both *Eucalyptus* species, a first set of sample plots was established using the most recent Spanish Forest Map, MFE25 (Miteco, 2011b), which contains species information. This step was aided by photointerpretation of the Worldview-3 images to discard any plots that clearly did not match the MFE25 map indications (i.e., due to land use changes or harvesting). The sample plots for each species encompassed different topographical orientations and slopes.

The field plots must represent homogeneous monospecific stands

with dense canopy closure. Within the provided sample plots, the center point of a circular plot, with a minimum radius of 10 m, was established and the main tree species was recorded. Considering that the forestry sector is quite active in the study area and that in several locations the tree species appearing on the MFE25 don't correspond with the ground truth, field crews were permitted to move the position of the proposed sample points to different nearby positions. This was done so as to maintain a roughly equal balance between the numbers of plots corresponding to each of the two species. The central coordinates of each plot that was ultimately established were recorded using a GPS device with centimetric precision.

Upon the collection of field data, polygons around the field plots were manually delineated using the Worldview-3 images as the reference. These polygons were used as reference data. A total of 395 polygons were defined: 215 for *E. globulus* and 180 for *E. nitens*. This reference dataset was randomly divided into two subsets: 70% for training and 30% for verification. Fig. 3 presents the distribution of the reference data, both training and test polygons.

4.2. Data processing

4.2.1. Shadow removal in Worldview images

The dataset of Worldview-3 images was visually reviewed to evaluate the influence of the heterogeneity of observation angles. It was observed that most of the images contained a great deal of projected shadows derived from the observation angle, which can greatly differ among the images. Therefore, the first step in data processing consisted of applying a shadow detection index (SDI) to every image that would allow for the removal of these shadows. The algorithm described by Shahi et al. (2014) was used. This index, which uses the blue band and the two NIR bands, was specifically designed for Worldview images. The following Eq. (1) is implemented to calculate the SDI.

$$SDI = ((NIR2 - Blue)/(NIR2 + Blue) - NIR1 \quad (1)$$

where NIR2, Blue and NIR1 are Worldview-3 bands.

Once the SDI was calculated for each pixel and each image, a histogram of the SDI frequencies was obtained for each image. A specific SDI threshold value for each image was defined to identify areas that corresponded to shadows. After several tests, the 95th percentile value, of each image, was selected as the optimum shadow threshold. Any values above this percentile were considered shadows and changed to NULL values.

4.2.2. Worldview texture analysis

A texture analysis was performed since, in very high-resolution images, textures can significantly differ between land covers (Feng et al., 2015). The first step consisted of defining the size of a moving window; all of the pixels within that window were used to obtain texture metrics. Several window sizes were tested. The results were visually inspected to select the appropriate window size. The final window size selected was 3x3 m. Afterwards, a histogram was computed for each window to determine the frequency of occurrence of each of the digital numbers (DN) present within the window and a vector with these occurrence values was created. The occurrence values were then normalized by dividing them by the total number of values in the defined moving window. These values were deemed probabilities, P(i). Finally, the following texture metrics were calculated from these probabilities by applying different equations: mean (2), variance (3), entropy (4), skewness (5). On this equations P(i) is the probability value of each pixel, Ng the number of distinct grey levels in the quantized image and M the mean.

$$\text{Mean}\,(M) = \sum_{i=0}^{Ng-1} iP(i) \quad (2)$$

$$\text{Variance} = \sum_{i=0}^{Ng-1} (i - M)^2 P(i) \quad (3)$$

$$\text{Entropy} = -\sum_{i=0}^{Ng-1} P(i)*\ln P(i) \quad (4)$$

$$\text{Skewness} = \sum_{i=0}^{Ng-1} (i - M)^3 P(i) \quad (5)$$

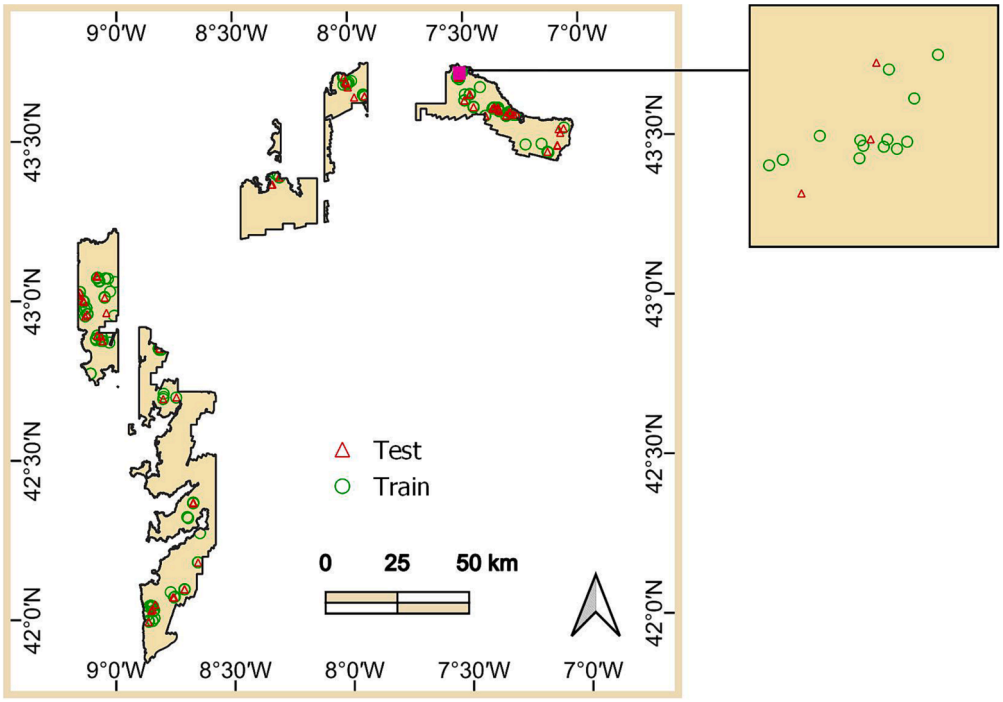

Fig. 3. Reference data distribution obtained through fieldwork. It was divided randomly into training data (TRAIN, 70%) and verification data (TEST, 30%).

The resulting value of each equation was assigned to the central pixel of the moving window. This procedure was performed for all the bands present in the image.

4.2.3. Sentinel-2 images

The Sentinel-2 images were pre-processed to remove any clouds that may be present. Clouds were masked using the cloud mask available from the Sentinel-2 Level 2A product. Since the bands used in this study were the 10 m and 20 m bands, the 20 m bands were resampled at 10 m. This procedure was done using nearest neighborhood interpolation.

Additionally several Sentinel-2 spectral indices were calculated since including them can improve the classification performance when mapping tree species using Sentinel-2 images (Immitzer et al. 2019). Some indices that are commonly used to analyze vegetation have been calculated. The Normalized Difference Vegetation Index (NDVI) (Kogan, 1995; Tarpley et al., 1984) was selected since it is the most commonly used index in phenological research (Misra et al. 2020). The Normalized Difference Moisture Index (NDMI) was used because according to previous studies it can track seasonal changes in vegetation moisture content (Gao, 1996; Sentinelhub, 2023a). Additionally, some indices that allow to optimize the Red-Edge bands of Sentinel-2 images were used. This band can be key to distinguish between vegetation species according to Misra et al. (2020). Particularly, the Normalized Difference Red Edge Index 1 (NDRE1) (Sentinelhub, 2023b) and the Sentinel-derived Red-Edge Spectral Indice RESI (Xiao et al. 2020) were used. Formulas to calculate them are presented below from (6)–(9) respectively.

$$NDVI = (NIR1 - RED)/(NIR1 + RED) \quad (6)$$

$$NDMI = (NIR1 - SWIR1)/(NIR1 + SWIR1) \quad (7)$$

$$NDRE1 = (RE2 - RE1)/(RE2 + RE1) \quad (8)$$

$$RESI = (RE3 + RE2 - RE1)/(RE3 + RE2 + RE1) \quad (9)$$

where NIR1, RED and SWIR correspond to the Sentinel-2 bands with equal names and RE1, RE2 and RE3 to the Sentinel-2 bands named Red-Edge 1, Red-Edge 2 and Red-Edge 3 respectively.

4.2.4. LiDAR data

Since the species in question can present different distribution patterns in terms of branches, sprouts, and the mix of different aged individuals, statistics were obtained from the LiDAR point clouds to derive information about the geometric structure of the stands. The first step was the normalization of the point clouds. This consisted of transforming the z coordinate value for each point from its altitude with respect to the Earth's surface to its height above the ground. To perform this transformation, ground points had to be identified. This step was performed with the *lasground* tool in the *LAStools* software (Rapidlasso, 2023). Then, the height of the rest of the points was estimated with respect to these ground points; this algorithm was implemented using the *lidR* package in the *R* software (Roussel et al., 2020).

The normalized LiDAR point cloud was used to estimate several statistical metrics representing the structure of the point clouds. The metrics computed are presented in Table 5; detailed mathematical information about each can be found in Roussel and Auty (2021). This step was performed using the *cloud metrics* function in the *lidR* package (Roussel et al., 2020). The set of metrics was calculated twice, once at a 1.2 m resolution (the Worldview-3 resolution) and once at a 10 m resolution (the Sentinel-2 resolution). The output of this process is nine raster layers, one layer per statistical metric.

4.3. Analysis of species separability

In this section, the separability of the two considered *Eucalyptus* species is analyzed separately for the three data sources. Boxplots of values for each species were built for Worldview spectral bands, Worldview textures and LiDAR statistics. The boxplots represent the mean values and central quartiles; they were built using the digital values for each feature of the pixels inside the reference polygons. Worldview separability was studied separately for each block given their divergences in the digital values as a result of the implementation of different pre-processing algorithms.

In the case of the Sentinel-2 data the separability between the species was analyzed through a temporal analysis of seasonal changes. This analysis was performed by analyzing the evolution of the monthly NDVI values along the considered year (2019) for both species; in particular the seasonal tendency was evaluated through the mean and standard deviation of the digital values in the reference polygons obtained for the monthly images.

Additionally the Jeffries-Matusita distance (JM) between the two species was calculated for all the data sources and variables. JM has been proven to be useful for measuring the separability of thematic classes obtained through remote sensing data (Sen et al. 2019). JM takes values between 0 and 2. Higher values indicate a higher separability between classes. JM was calculated using the R function *JMdist* from the *R* package *varSel* (Dalponte and Oerka, 2021).

Table 5
LiDAR metrics obtained.

Metric	Description
zmax	Maximum height
zmean	Mean height
zsd	Standard deviation of height distribution
zskew	Skewness of height distribution
zentropy	Entropy of height distribution, calculated as the normalized Shannon diversity index (Pretzsch, 2008; Shannon, 1948)
pzabovezmean	Percentage of returns above mean height
pzabove2	Percentage of returns above 2 m
zqx	x^{th} percentile of height distribution
zpcumx	Cumulative percentage of returns in the x^{th} layer. In order to obtain this layer, the maximum height of the LiDAR data in each cell was divided into 10 intervals. The cumulative percentage of the 9 layers was thus obtained.

4.4. Species classification

The detection and mapping of *E. globulus* and *E. nitens* in the study area was accomplished through supervised classifications of the data from the different sources, which were treated both individually and combined.

Since the dates of the different phenological stages differ from one target species to the other, the temporal resolution of the Sentinel-2 data was used to design the tests used to differentiate between the two species. One image per month was selected and classified individually using the Sentinel-2 spectral bands (this was deemed the single-date approach). A multitemporal approach was also evaluated; it consisted of using decision-criteria to aggregate all the maps resulting from the single-date approach. The decision-criteria used was plurality voting (Lewiński et al., 2017). Following this criterion, the most frequently occurring class for a pixel (the mode) throughout the time-series was the class that was ultimately assigned to that pixel in the multitemporal map.

Regarding Worldview-3, three tests were performed: the classification of the images individually, the classification of textures, and the classification of the two together. In the first case, the classification was performed separately for the two blocks of images. This was because, due to differences in the corrections applied within the blocks, the blocks presented quite different radiometric ranges (see Section 3.1.). The separation of blocks was not necessary in the case of the textures since these were obtained from normalized values.

Finally, the LiDAR metrics were analyzed individually and combined

with the Sentinel-2 and Worldview-3 images. Table 6 is a description of all the different data combinations used.

Supervised classifications were performed using the training data described in Section 4.1. These were performed using a neural network architecture. The architecture used was implemented using the *Keras* interface (Team, 2022) from the *TensorFlow* library (Abadi et al., 2016) of the *Python* language (Van Rossum and Drake, 1995). Several neural network architectures were tested. The one that was ultimately used consisted of an input flatten layer, three dense hidden layers, and an output layer. The hidden layers were activated with the *ReLU* (Rectified Linear Units) activation function (Agarap, 2018). This activation function is one of the most efficient functions for this step (Ramachandran et al., 2017). The output function used was *Softmax* (Agarap, 2018) since it was a matter of multiclass classification (Wu et al., 2016). As a result of this process, a map with the geospatial distribution of *Eucalyptus globulus* and *Eucalyptus nitens* was obtained from each of the data sources evaluated.

The final step was to evaluate all the obtained maps using the verification dataset. Confusion matrixes were built for each of the maps to estimate the following accuracy metrics: Overall Accuracy (OA), User's Accuracy (UA), Producer's Accuracy (PA) and F-Score.

5. Results

5.1. Analysis of species separability

5.1.1. Worldview images

The boxplots showing the separability of the species according to the Worldview bands are shown in Figs. 4 and 5, block 1 and 2 respectively. The Figures incorporate the JM values obtained for each band. According to these results, the digital values in the Worldview images overlap for the analyzed species whatever the spectral band or block is considered. Accordingly, JM values are always below 0.5. However JM values within blocks are completely different. The highest JM value obtained for these images corresponds to the NIR-2 band in block 1 (JM 0.41).

5.1.2. Textural analysis

The boxplots and the JM distances showing the species separability considering the textural raster layers derived from the Worldview bands are shown in Fig. 6 for block 1 and on Fig. 7 for block 2. For the block 1 the highest JM values were obtained for the skewness and mean textures; particularly the Yellow and the NIR-1 bands presented the highest values: 0.98 and 0.76 respectively. The results are different in the block 2. In this case the skewness presented the best performance, corresponding the highest values to the Red and Coastal bands: 0.86 and 0.72 respectively.

Table 6
Data sources and their combinations.

Name	Description of the data source
LiDAR_1.2m	LiDAR metrics derived at a 1.2 m resolution.
LiDAR_10m	LiDAR metrics derived at a 10 m resolution.
WV3	Worldview bands.
TEXTURES	Textural metrics from Worldview.
WV3_LiDAR	Worldview bands and LiDAR metrics derived at a 1.2 m resolution.
WV3_TEXTURES	Worldview bands and textural information.
LiDAR_TEXTURES	LiDAR metrics derived at a 1.2 m resolution and textural metrics.
WV_LiDAR_TEXTURES	Worldview bands, LiDAR metrics derived at a 1.2 m resolution and textural metrics.
S2_MULTI	Sentinel-2 bands, multitemporal aggregation.
S2_MONTH	Sentinel-2 bands, for each of the 12 months.
S2_LiDAR_MULTI	Sentinel-2 bands and LiDAR metrics derived at a 10 m resolution, multitemporal aggregation.
S2_LiDAR_MONTH	Sentinel-2 bands and LiDAR metrics derived at a 10 m resolution, for each of the 12 months.

5.1.3. Sentinel-2 images

The result of the seasonal changes tendency is presented in Fig. 8. According to this Figure NDVI mean values of both species are very similar from January to March. From April to November the mean NDVI is higher for *E. nitens*. However, the standard deviation of the NDVI values result in overlapped confidence intervals across the whole year.

The resulting values of the JM distance obtained for the Sentinel-2 bands and spectral indices are presented on Fig. 9 and Fig. 10. In all the cases, the JM value is below 0.8. The highest values correspond to the RGB bands; they overtake the value 0.6 at least once in the year. The months for which JM values are above 0.6 are May and November. Among the spectral indices used, the ones that presents higher JM values are NDVI, the NDRE1 and the RESI for September. Regarding the NDMI, generally it presents lower values than the other indices for all months except in February and March.

5.1.4. LiDAR data

The boxplots showing the separability of the species through the LiDAR metrics are shown in Fig. 11. According to this figure, there are several LiDAR metrics whose values differ noticeably between the two species: "zmax", the higher height percentiles and "zsd". For example, in the study area, according to "zmax", *E. globulus* stands tend to be taller than *E. nitens* stands: for *E. globulus,* "zmax" has an average value of 21.3 m, with a standard deviation of 6.20 m, while for *E.nitens* "zmax" has an average value of 15.2 m with a standard deviation of 4.87 m. The variables "zmax", "p75" to "p95" and "zsd" have the highest JM values; they range between 0.49 and 0.55.

5.2. Species classification

The accuracy metrics of the maps obtained using the different data sources and the various combinations of them are shown in Figs. 12 and 13. The Fig. 12 shows the Overall Accuracy obtained for each classification. The highest values, as in the previous case, were obtained with for the March Sentinel-2 image combined with LiDAR (with an OA of 94%) followed by Sentinel-2 multitemporal (with an OA of 92%). Furthermore, the OA index also revealed that Sentinel-2 images provided more accurate results when they were combined with LiDAR data. It should be highlighted that the months that allowed for the highest accuracy values were in the spring months of March and May. The accuracy was lower in summer and winter months. Finally, among the high-resolution combinations, Worldview-3 image with textures and LiDAR data provided the highest OA, with a value of 90%.

Fig. 13 presents the F-Score obtained for each of the classifications of the two species. It is worth noting that although Worldview-3 with textures and LiDAR data has a high OA, there is an imbalance between the F-Score of the two classes. It seems that the *E. globulus* class tends to be more accurately predicted than the *E. nitens* class. This disparity is observed in most of the combinations that include Worldview data or data at Worldview resolution. Producer's and User's accuracies are presented on Appendixes A and B respectively.

Finally, Fig. 14 shows the distribution of both species in the study area according to the classification that allowed to obtain a higher OA, Sentinel-2 March image combined with LiDAR data.

6. Discussion

6.1. Analysis of species separability

6.1.1. Worldview images

The separability of the analyzed species considering the Worldview-3 spectral bands seems to be low since most JM values are below 0.5. The most remarkable observation is that the JM values highly differed between blocks. This difference might be related to the phenology of the

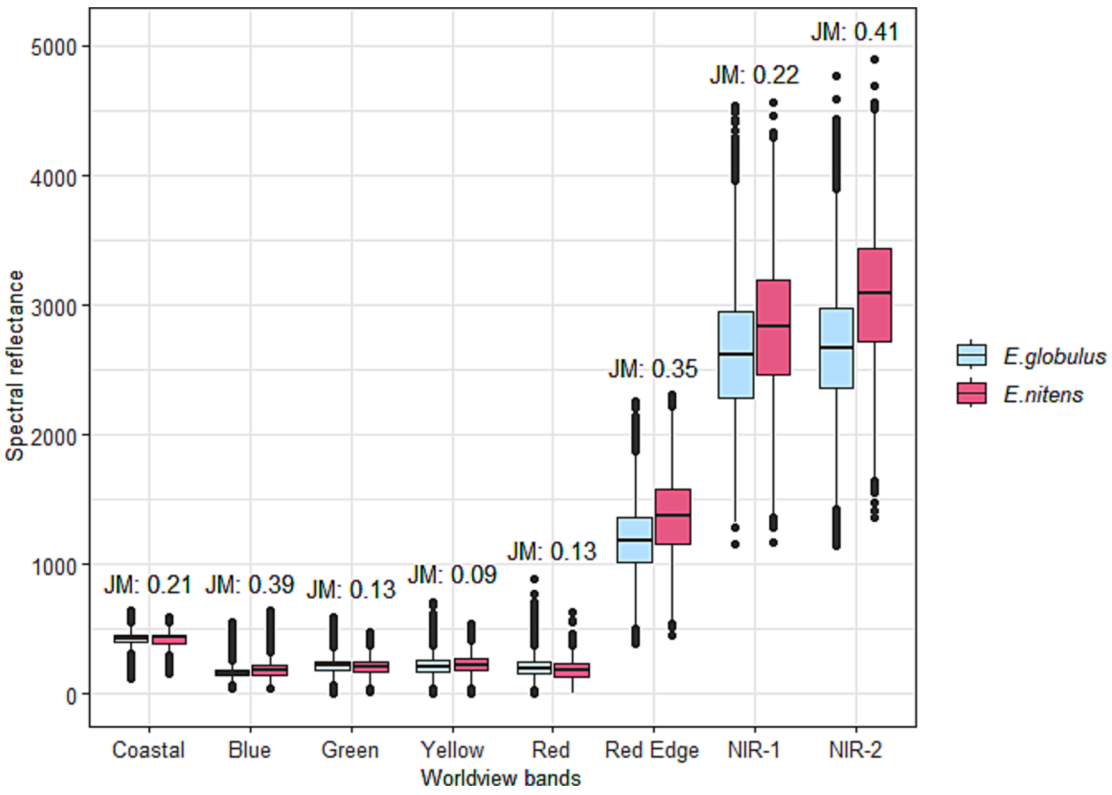

Fig. 4. Boxplot of Worldview-3 band values reflected by *E. globulus* and *E. nitens* for Block 1. JM indicates Jeffries-Matusita distance values obtained for each variable.

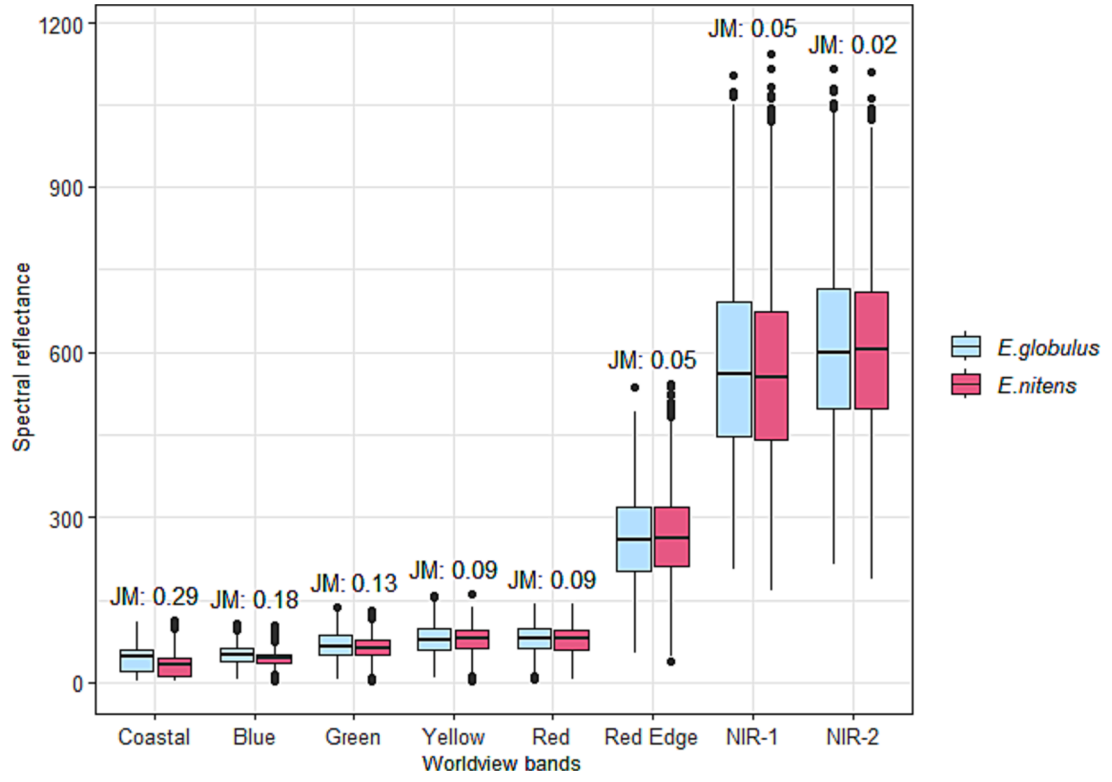

Fig. 5. Boxplot of Worldview-3 band values reflected by *E. globulus* and *E. nitens* for Block 2. JM indicates Jeffries-Matusita distance values obtained for each variable.

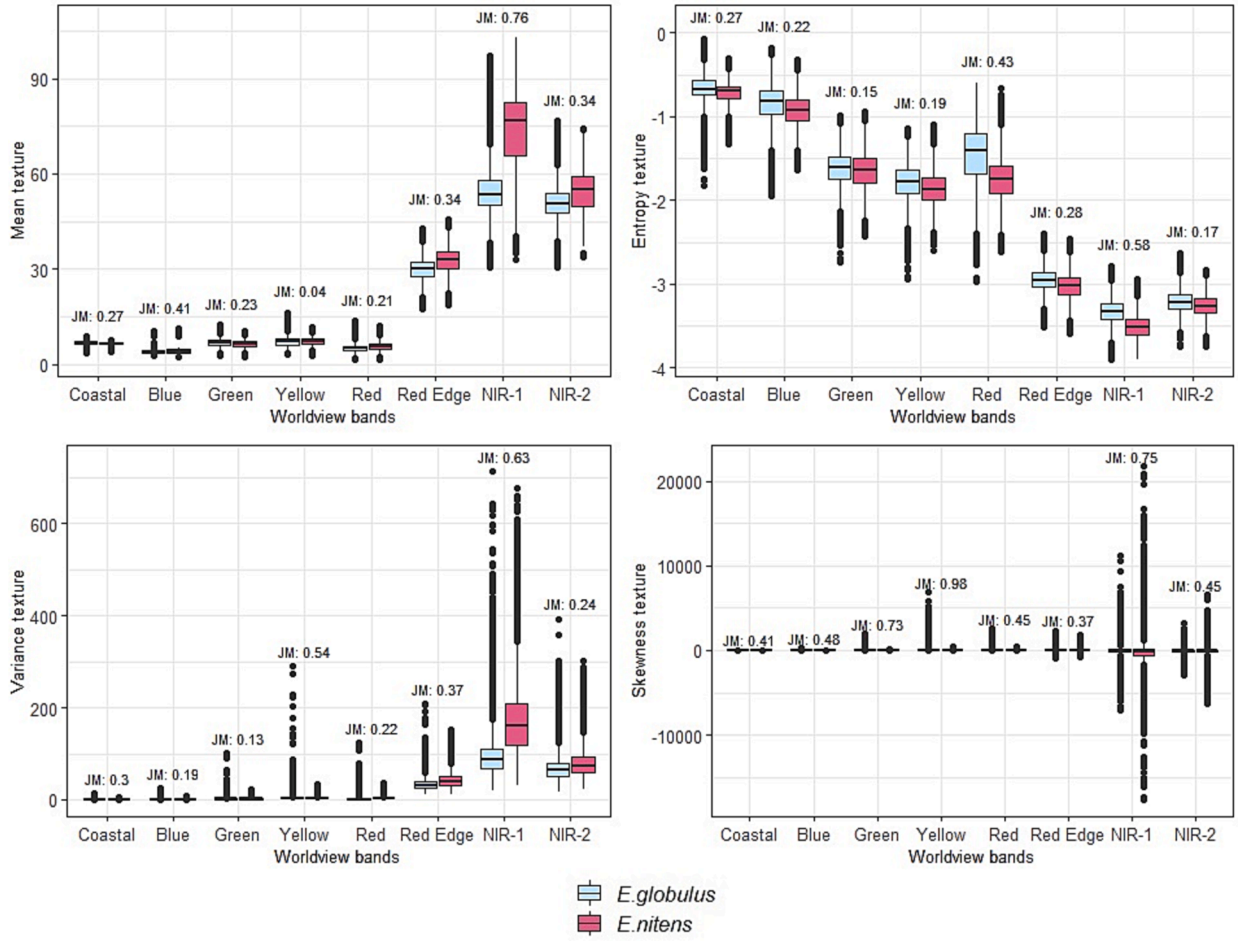

Fig. 6. Boxplot of Worldview-3 textural metrics of *E. globulus* and *E. nitens* for block 1. JM indicates Jeffries-Matusita distance values obtained for each variable.

species, since the block with the best performance includes those months when the emergence of shoots occurs (spring). Considering this result, the training data collection for further classifications should not combine different dates since it might difficult the construction of the model.

Regarding Worldview-3, it also might be pointed out that the radiometric inconsistency among blocks might difficult obtaining full conclusions regarding the application of Worldview-3 images to large areas.. Further studies to disentangle this problematic might be essential to fully address the potential of Worldview-3 images at large scales.

6.1.2. Textural analysis

The best separability results for the analyzed species was obtained for the Worldview-3 texture metrics with JM values close to 1. The best performance corresponded to the skewness of the yellow band in block 1 (JM 0.98) and the skewness of the red band in block 2 (JM 0.86). Skewness is one of the texture metrics more sensitive to the presence of extreme values. Therefore, it will be a metric sensitive to small canopy gaps, brighter or darker pixels in the middle of the canopy. This might indicate that one species is more prone to have canopy gaps, due to its crown structure or plantation pattern, than the other. Nevertheless, it might be also considered that this metric is also really affected by the presence of outliers derived from, for example, edge pixels or unremoved shadows.

Textural analysis results contrast with Chen et al. (2021); they obtained that the mean texture was the most valuable one to differentiate *Eucalyptus* plantations from other tree covers. This variation between studies might derive from the differences on structure of the specific species of each study, since different crown structures tend to lead to different key textural metrics (Ouma and Tateishi, 2007). For example, Franklin and Ahmed (2018) found relevant different textural features to classify each one of the four broadleaves species that composed their study. Considering this, results might highly differ among the species studied as well as between interspecific or intraspecific studies.

6.1.3. Sentinel-2 images

The separability between *E. globulus* and *E. nitens* through the Sentinel-2 bands and indices can be considered low considering that JM distances are under 1 for them all whatever the month is analyzed. This value is the threshold to consider that a dataset show potential for classes differentiation according to Sen et al. (2019). It highlights that the highest JM values were obtained for the blue, green and red bands (RGB) in November. Analyzing this result in detail it was observed that RGB values on November present outliers which correspond to cloud shadows. Hence, to improve the results, the outliers might be filtered prior the JM distances calculation.

It might be pointed that Sentinel-2 bands allow to obtain JM distances above 0.5, whereas spectral indices tend to be below 0.5. This result contrasts with other studies as Immitzer et al. (2019) or Xiao et al. (2020) which indicate that including spectral indices to species classification studies aggregates separability potential. The highest JM distances for spectral indices correspond to September while for spectral bands to May and November. The indices that present highest values in most months are the NDRE1 and the RESI, what agrees with previous studies as Misra et al. (2020) or Xiao et al. (2020) which highlights the potential of Red-Edge bands of Sentinel-2 images to distinguish among vegetation types. The NDMI only present high values in February and March which can indicate that in this period one of the two species

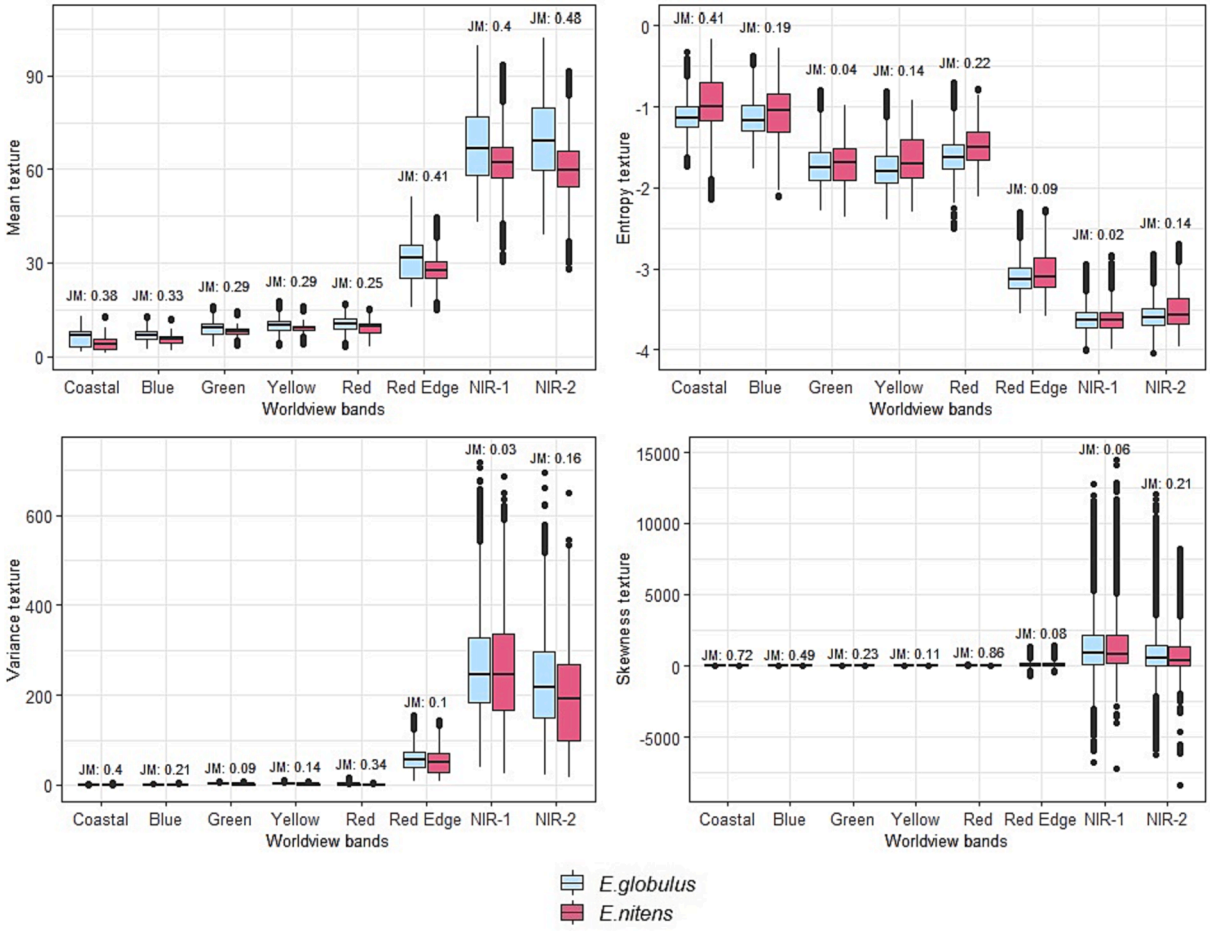

Fig. 7. Boxplot of Worldview-3 textural metrics of *E. globulus* and *E. nitens* for block 2. JM indicates Jeffries-Matusita distance values obtained for each variable.

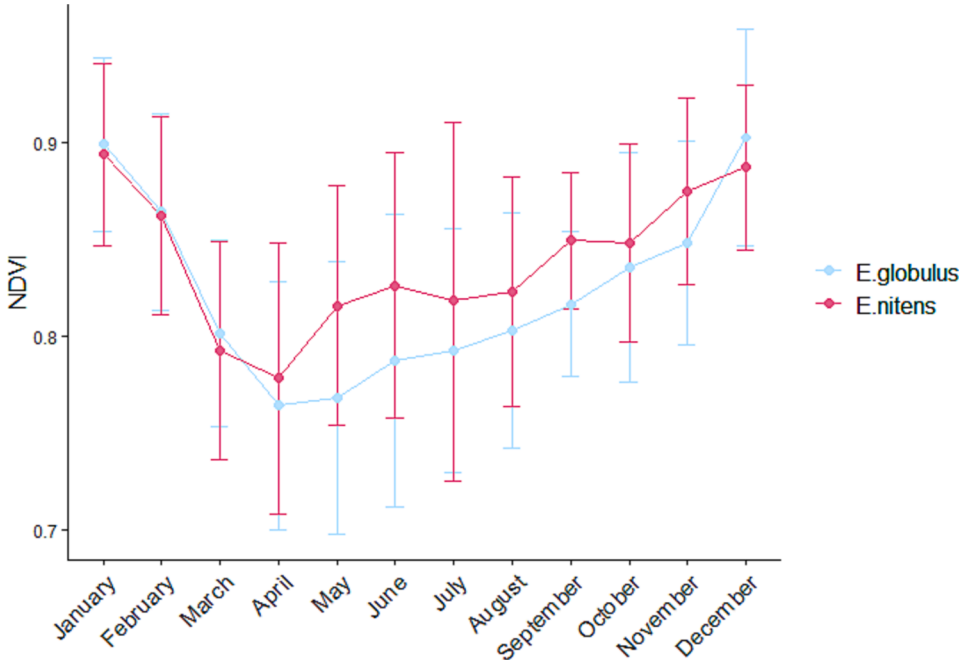

Fig. 8. Evolution of the NDVI for *E. globulus* and *E. nitens* along the year 2019. It is calculated from Sentinel-2 monthly images.

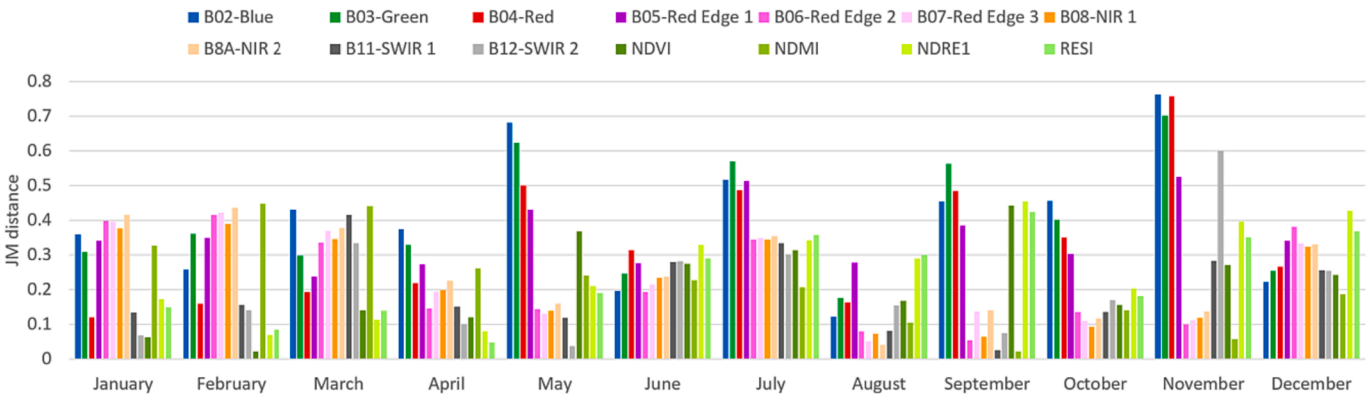

Fig. 9. Jeffries-Matusita distances (JM) for each Sentinel-2 band and spectral index, and for every month, to measure the separability between *E. globulus* and *E. nitens*.

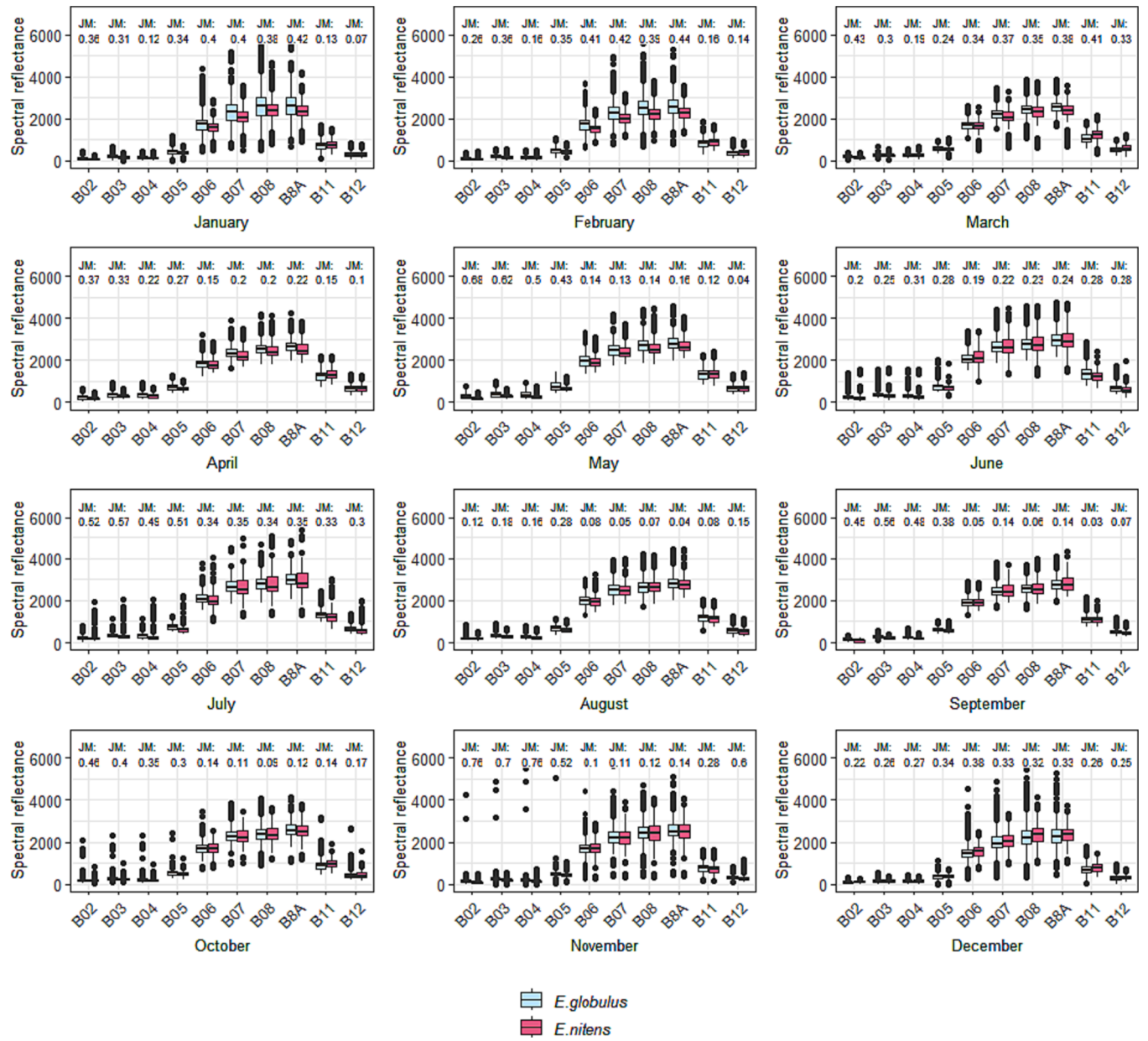

Fig. 10. Boxplot of Sentinel-2 bands of *E. globulus* and *E. nitens* for every month. JM indicates Jeffries-Matusita distance values obtained for each variable.

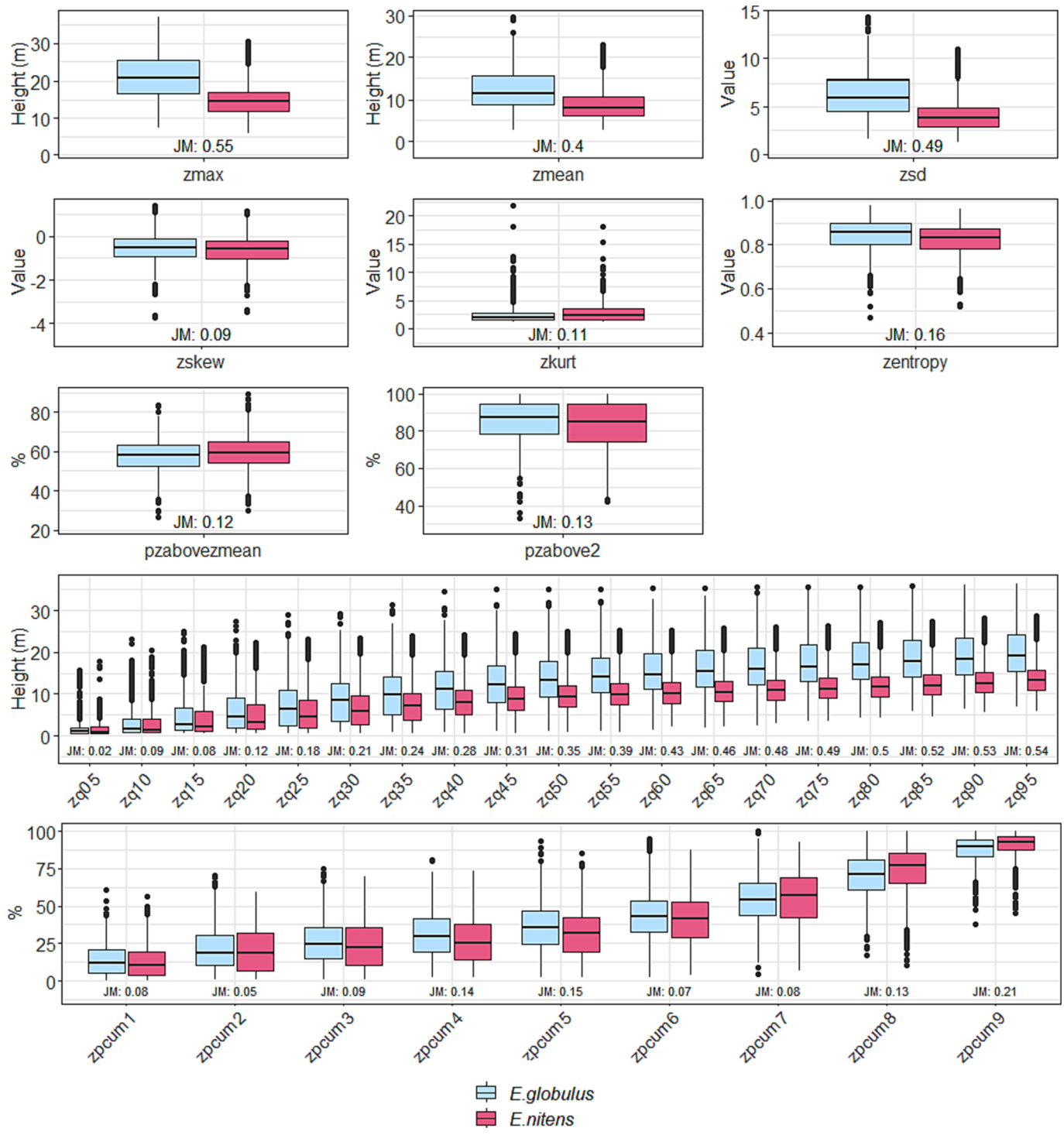

Fig. 11. Boxplot of LiDAR metrics calculated at 10 m for *E. globulus* and *E. nitens*. JM indicates Jeffries-Matusita distance values obtained for each variable.

maintains a higher water content than the other, since this index is focused on the moisture of the vegetation (Gao, 1996). Further studies should be done to better understand the winter-spring strategy of both species.

The analysis of the evolution of the NDVI through time has shown that the mean values for both species mostly differ in May and June, but the confidence intervals are overlapped along the whole year. An important observation is that months with similar NDVI mean values presented high overall accuracy in the final classification. Considering these results this index seems not to be efficient to capture key spectral differences related to the phenology of the analyzed species; consequently future studies should be done to find another feature that reflect the seasonal changes of these species. Nevertheless, NDVI values decreases from January to April and they start to recover again from May onwards. This might be due to the appearance of new buds since spring months are associated with the peak budding for both species. Also, according to NDVI values it seems that *E. globulus* has lower photosynthetic activity than *E. nitens* (lower NDVI values in *E. globulus*). However, the current knowledge about the phenology of both species (i.e. response to temperature) is too scarce to allow the authors explaining

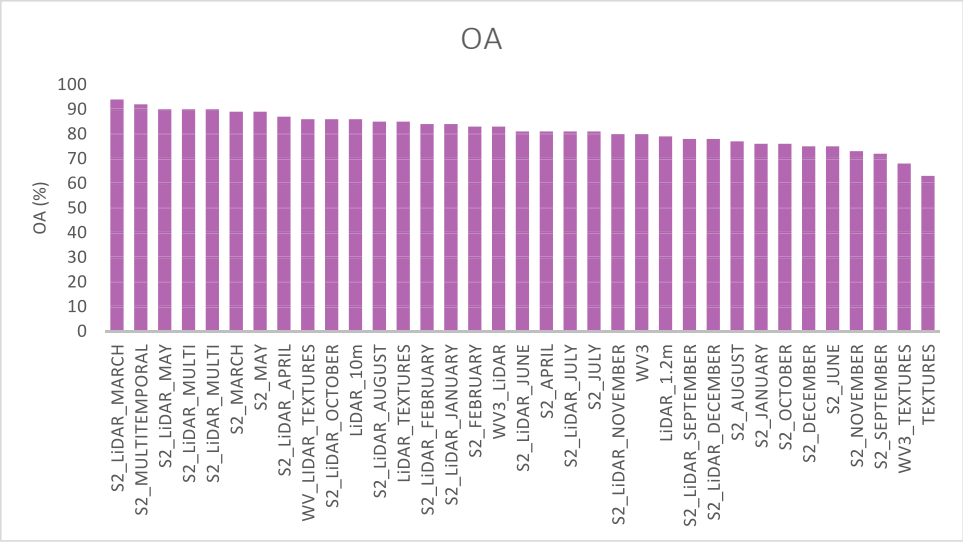

Fig. 12. Overall Accuracy obtained for the classifications performed.

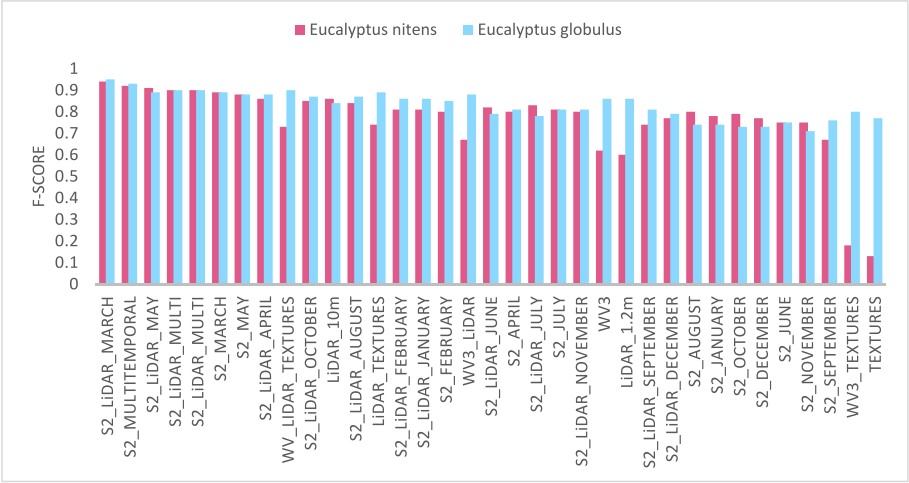

Fig. 13. F-Score obtained for the classifications performed.

conclusively this behavior. Field work should be done to better understand the relation of the monthly NDVI values with the phenology of both species on the study area. An improvement of the knowledge of the phenological behaviour of both species might help to improve their monitoring.

6.1.4. LiDAR data

The LiDAR metrics that seem to have the greatest capability to discern between the analyzed species are “zmax”, “p75” and “p95”. It might be noted that they are clearly related to height of the trees, but not to their structure (i.e. natural pruning). Yadav et al. (2021) and Verma et al. (2019) have also pointed that tree height can help to distinguish between *Eucalyptus* species. However, as Verma et al. (2019) pointed out the importance of height related variables can be related to the maturity stage of the studied stands, which are circumstantial conditions. Consequently every site and stand might be evaluated specifically. In this specific study case, the height of the *E. globulus* stands could tend to be higher than the height of *E. nitens* stands considering that most plantations of *E. nitens* date from the last two decades (Pérez-Cruzado and Rodríguez-Soalleiro, 2011) while *E. globulus* was previously introduced, and that there are records in numerous locations that point that *E. globulus* stands fell in abandonment for decades (Tomé et al., 2021). Hence, the utility of LiDAR data in differentiation and mapping of this two *Eucalyptus* species may change in the upcoming years. Therefore, a study similar to this one might be done again selecting for the analysis stands with equal ages.

6.2. Species classification

Despite the modest results of the separability analysis, according to the obtained results *E. globulus* and *E. nitens* can be satisfactorily differentiated in the study area through supervised classification. The data source that provided the highest accuracy metrics was Sentinel-2 combined with LiDAR data (OA 94%) followed by the multitemporal approach of Sentinel-2 (OA 92%). This is fortunate since Sentinel-2 is an open-access source, and its availability is guaranteed in the coming years (Toulemont et al., 2021). An important finding regarding this source is that the date of the image analyzed is a key parameter in determining the final accuracy of the map, and consequently, in the capability of Sentinel-2 images to differentiate between *Eucalyptus* species. In the study area, the spring months, March and May in particular, provided the highest accuracy metrics (OA 89% for both months). These months might correspond with a key phenologic stage of the species analyzed, emergence of spring shoots, since according to BASOA

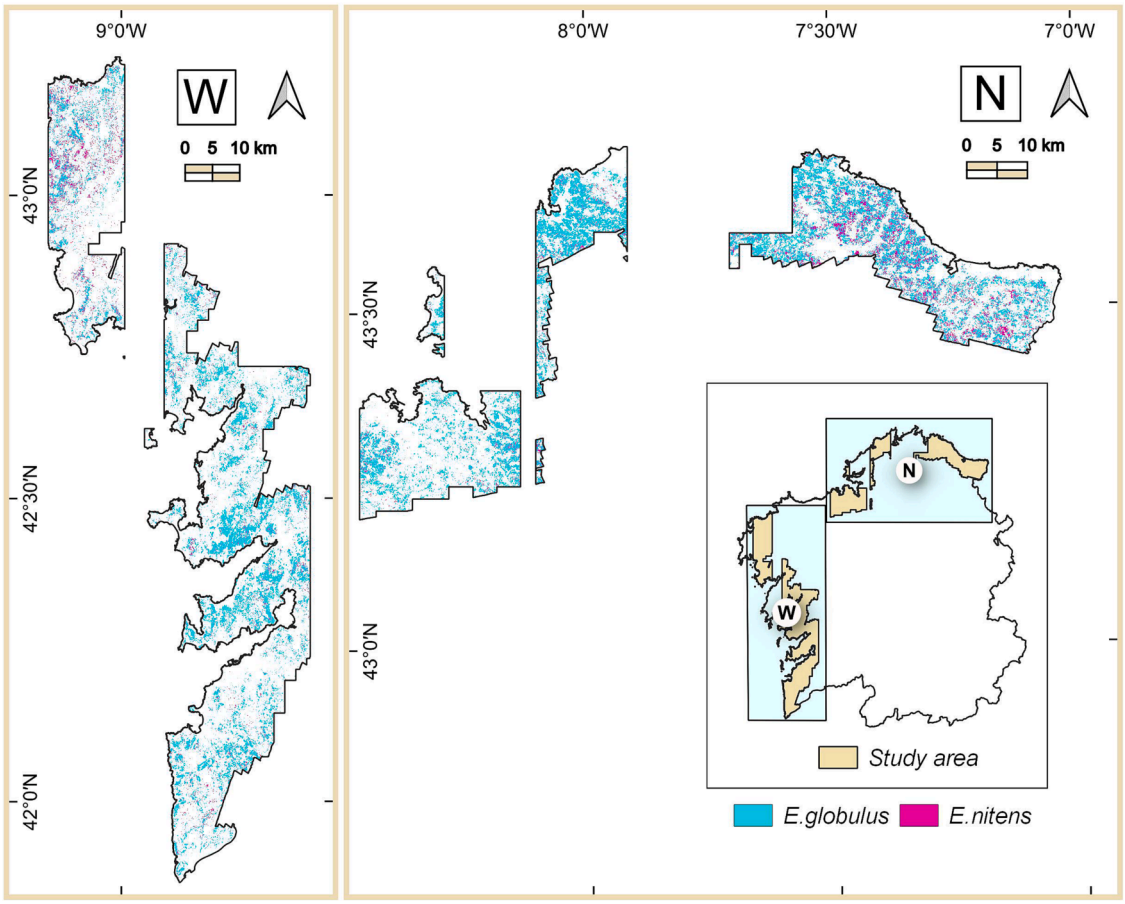

Fig. 14. *Eucalyptus* species classification result for Sentinel-2 March image combined with LiDAR data.

Foundation (2017), spring shoots in *E. globulus* tend to exhibit a greenish coloration, while those of *E. nitens* tend to show reddish tones. Having this in mind it would be of great interest to increase the knowledge of both species phenology in the region as well as to go deep on how to take advantage of this behavioral differences using remote sensing.

It might also be remarked that the multitemporal approach provided better results than almost all the single-date images both when they were processed alone and combined with LiDAR. This is in accordance with the previous studies on tree species classification as for example Immitzer et al. 2019 or Persson et al. 2018 that indicate that multitemporal classifications provide higher accuracy than single dates ones. In fact, some previous studies had already analyzed the phenological behavior of *Eucalyptus* through remote sensing with the aim of classifying the genera (Qiao et al., 2016; Forstmaier et al., 2020). Future studies could explore the possibility of applying plurality voting using only the months with the highest accuracy values, for example by combining the results from only March, April, and May. This approach would strengthen the phenology-based differentiation, since phenology may vary within these months depending on the geographical area (i.e., they may be different in coastal areas versus inland areas) as it happens with other tree species in the study region (Rodríguez-Rajo et al. 2011).

The low accuracy results obtained with Worldview-3 images when they were processed alone are similar to the results obtained in Alonso et al. (2022). They also reported disparities in accuracy metrics between species when using a Worldview-3 image dating from July. For example, in their study, the UA for *E. nitens* was 65% while it was 70% for *E. globulus*. They pointed out that this may be due to an imbalance in species distribution, and in training data in their study area. In the current study there is no imbalance between species in the training data, however the accuracy remains low: the UA for *E. nitens* and *E. globulus* in this study was 61% and 87% respectively and the PA was 62% and 86%. Hence *E. nitens* was more underestimated than *E. globulus* when using Worldview-3, as well as *E. globulus* was more commonly misclassified.. Some other studies were able to efficiently differentiate between *Eucalyptus* species. This is the case of Peerbhay et al. (2014), that focused in the differentiation and mapping of *E. grandis*, *E. nitens* and *E. smithii* in South Africa using Worldview images. Therefore, the efficiency of this data source could depend greatly on the species in question, since, as previously studied, some *Eucalyptus* species present very similar spectral reflectance (Kumar, 2007; Datt, 1999). *E. globulus* and *E. nitens* are closer from a phylogenetic point of view than for example *E. nitens* and *E. grandis* (Bayly, 2016).

It should be highlighted that the combination of Worldview-3 spectral information and LiDAR data with Worldview-3 textural metrics yielded more accurate results. This result is in accordance with Verma et al. (2019), who observed that textural information helped to differentiate between some *Eucalyptus* species in their native environment. Enhancements observed when including Worldview-3 textural information were related, on other trees species classification studies, with the possibility that texture offer to capture species-specific differences in crown-structure (Pinheiro Ferreira et al., 2019). In view of this result, it might be possible that a slight difference on structures of both species not previously recorded exists. Other possible is that textural differences derive from different stand structures driven from the higher abandonment rate of *E. globulus* stands (Tomé et al., 2021).

The comparison of Sentinel-2 and Worldview-3 has brought to light certain issues regarding the efficiency of the two sources in the E. *globulus* and *E. nitens* mapping. In general, Sentinel-2 images provided higher accuracy metrics solely (OA 92% in the best case) than Worldview-3 (OA 80% in the best case). This better performance could

be due to that Sentinel-2 images have higher radiometric and temporal resolutions. It should be noted that not all the Worldview-3 images date from months that correspond with the emergence of spring shoots. These results could be substantiated if the Worldview-3 images could be acquired for the whole study area during the optimum phenological period; it would also allow to decipher if the higher accuracy obtained with Sentinel-2 is driven by the multitemporality or by the higher spectral resolution. However, nowadays the operational constraints of Worldview-3 satellite hinder its capacity to cover large areas in a narrow time frame, consequently the availability of Worldview-3 images in the required period with a low cloud threshold is currently difficult.

Regarding the LiDAR data, it was observed that LiDAR data alone can be useful to distinguish between the two species when it is used at medium resolutions (a 10 m resolution yields more accurate results than a 1.2 m resolution). This may indicate that using LiDAR with low resolutions involve the inclusion in training and test areas of noisy pixels that correspond to areas not covered by the tree canopy. As a consequence, the LiDAR statistics of those pixels would correspond to shrubs instead of to *Eucalyptus* trees. This feature would greatly interfere with the results. The review on tree species classification of Fassnacht et al. (2016), indicates that low density discrete return LiDAR alone has a limited potential for tree species classification. This contrast with the result of this study. This discrepancy might be due to the values of height related parameters in both species in the study area. This reinforces the need of evaluating every site specifically.

The combination of LiDAR data with multispectral data facilitated the differentiation between the two *Eucalyptus* species. This is in accordance with Verma et al. (2019) and Yadav et al. (2021) who found that LiDAR leveraged the potential of multispectral images to classify *Eucalyptus* species in their native environment.

7. Conclusion

This study reveals that Sentinel-2 images have a great potential to efficiently differentiate between *E. globulus* and *E. nitens* and map their distribution. The date of the images analyzed is a key parameter in determining the final accuracy of the map; in particular, the emergence of spring shoots period is the best phenological stage to capture in Sentinel-2 images in order to differentiate between these two species. The classification following a multitemporal approach can optimize the accuracies obtained. LiDAR metrics can also be used to complement the models and improve results. However, the LiDAR derived metrics can be greatly influenced by the local and circumstantial conditions of the stands of both species in the study region. LiDAR data alone may have the potential to differentiate between the two species but when it is used at medium resolutions. Worldview-3 images alone have a low potential to differentiate between the two species. Including textural information leverages their potential but their prediction capabilities remain low. Furthermore, this study details the difficulties that working with Worldview-3 data at large scales might entail.

This study represents a step forward in terms of obtaining updated *Eucalyptus* species distribution maps for Europe, a feat which will add to the current knowledge base and allow for forest and conservation stakeholders to plan better and make more informed decisions. In line with the results obtained in this study, and due to the easy accessibility of Sentinel-2 images, future studies should focus on upscaling this study using Sentinel-2 images to obtain a definitive map for this region.

Funding

This project was funded by the Administration of Rural Areas of the Government of Galicia under Grant 2020CONVINVENTARIOFORESTALR002; by the Spanish Ministry of Sciences, Innovation and Universities under the grant FPU19/02054; Spanish Ministry of Sciences, Innovation and Universities under grant PID2019-111581RB-I00 project PALEOINTERFACE: STRATEGIC ELEMENT FOR THE PREVENTION OF FOREST FIRES, DEVELOPMENT OF MULTISPECTRAL AND 3D ANALYSIS METHODOLOGIES FOR INTEGRATED MANAGEMENT.

Funding for open access charge: Universidade de Vigo/CISUG.

CRediT authorship contribution statement

L. Alonso: Conceptualization, Data curation, Formal analysis, Investigation, Methodology, Funding acquisition, Supervision, Validation, Visualization, Writing – original draft, Writing – review & editing. **A. Rodríguez-Dorna:** Data curation, Formal analysis, Investigation, Visualization, Writing – review & editing. **J. Picos:** Conceptualization, Funding acquisition, Project administration, Resources, Supervision, Validation. **F. Costas:** Software, Data curation. **J. Armesto:** Conceptualization, Funding acquisition, Project administration, Resources, Validation, Writing – review & editing.

Declaration of Competing Interest

The authors declare that they have no known competing financial interests or personal relationships that could have appeared to influence the work reported in this paper.

Appendix A. . Sentinel-2 images used in the study. The heading of each column indicates the Sentinel-2 tile. Below each heading, the dates of the images are shown

	TILES				
	TMH	TNH	TPJ	TNG	TNJ
DATES	2019-01-03	2019-01-08	2019-01-05	2019-01-10	2019-01-05
	2019-02-12	2019-02-12	2019-02-14	2019-02-14	2019-02-12
	2019-03-29	2019-03-29	2019-03-26	2019-03-21	2019-03-24
	2019-05-03	2019-04-28	2019-04-20	20190–4-30	2019-04-28
	2019-05-13	2019-05-13	2019-05-30	2019-05-05	2019-05-13
	2019-05-28	2019-05-28	2019-07-19	2019-05-30	2019-07-12
	2019-07-22	2019-07-12	2019-07-24	2019-07-19	2019-07-24
	2019-08-21	2019-08-16	2019-08-23	2019-08-13	2019-08-16
	2019-09-15	2019-09-15	2019-09-12	2019-09-12	2019-09-15
	2019-10-10	2019-10-10	2019-10-07	2019-10-07	2019-10-10
	2019-12-04	2019-12-04	2019-11-21	2019-10-22	2019-11-29
	2019-12-29	2019-12-29	2019-12-26	2019-12-29	2019-12-04

Appendix B. . Producer's accuracy obtained for the classifications performed

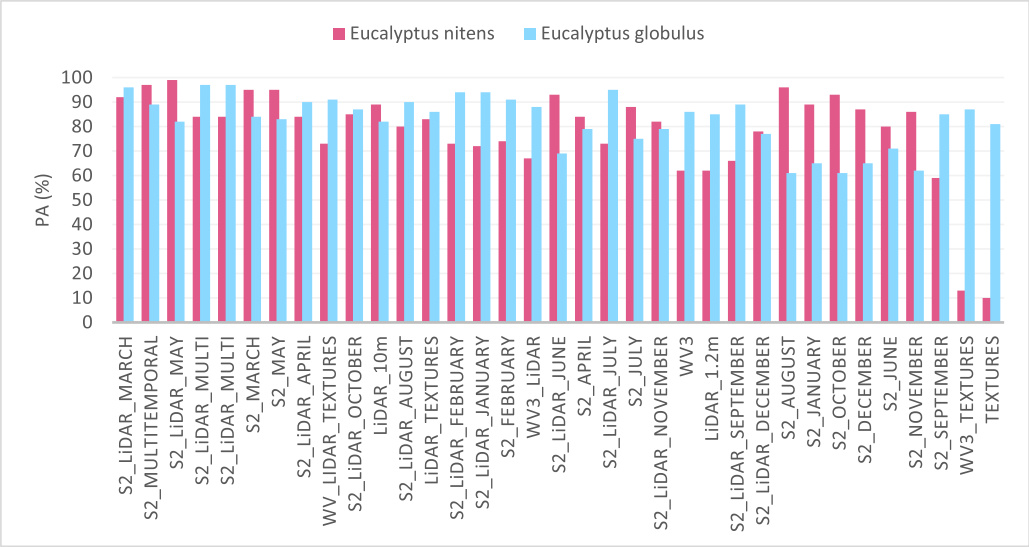

Appendix C. . User's accuracy obtained for the classifications performed

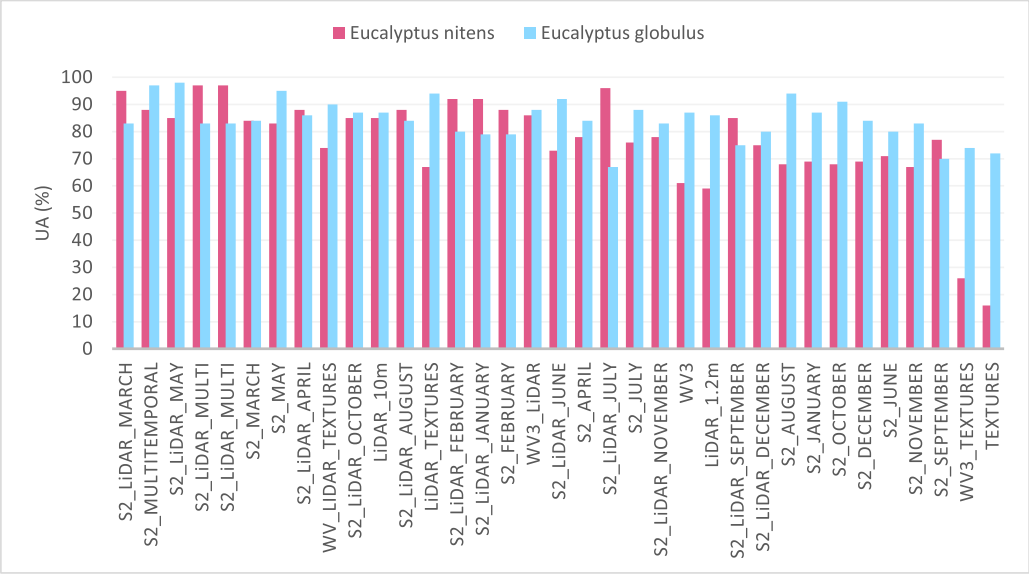

References

Abadi, M., Agarwal, A., Barham, P., Brevdo, E., Chen, Z., Citro, C., Corrado, G. S., Davis, A., Dean, J., Devin, M., Ghemawat, S., Goodfellow, I., Harp, A., Irving, G., Isard, M., Jia, Y., Jozefowicz, R., Kaiser, L., Kudlur, M., … Zheng, X., 2016. TensorFlow: Large-Scale Machine Learning on Heterogeneous Distributed Systems. arXiv. https://doi.org/10.48550/ARXIV.1603.04467.

Acuña, L., Sepliarsky, F., Spavento, E., Martínez, R.D., Balmori, J.-A., 2020. Modelling of impact falling ball test response on solid and engineered wood flooring of two eucalyptus species. Forests 11. https://doi.org/10.3390/f11090933.

Agarap, A.F., 2018. Deep Learning using Rectified Linear Units (ReLU). arXiv. <https://doi.org/10.48550/arXiv.1803.08375>.

Aguín, O., Sainz, M.J., Ares, A., Otero, L., Pedro Mansilla, J., 2013. Incidence, severity and causal fungal species of Mycosphaerella and Teratosphaeria diseases in Eucalyptus stands in Galicia (NW Spain). For. Ecol. Manag. 302, 379–389. https://doi.org/10.1016/j.foreco.2013.03.021.

Alonso, L., Picos, J., Armesto, J., 2021a. Forest land cover mapping at a regional scale using multi-temporal sentinel-2 imagery and RF models. Remote Sens. 13, 2237. https://doi.org/10.3390/rs13122237.

Alonso, L., Picos, J., Armesto, J., 2021b. Forest cover mapping and Pinus species classification using very high-resolution satellite images and random forest, ISPRS Ann. Photogramm. Remote Sens. Spatial Inf. Sci. 3, 203–210. https://doi.org/10.5194/isprs-annals-v-3-2021-203-2021.

Alonso, L., Rodríguez, A., Picos, J., Armesto, J., 2022. Challenges in automatic forest change reporting through land cover mapping. Forest.: Int. J. Forest Res. 96, 155–169. https://doi.org/10.1093/forestry/cpac053.

Antes, R., Joutsimo, O.P., 2015. Fiber Surface and Paper Technical Properties of Eucalyptus globulus and Eucalyptus nitens pulps after modified cooking and bleaching. BioResources 10 (1), 1599–1616.

Arenas, S., Rodríguez-Soalleiro, R., Diaz-Balteiro, L., 2019. Turno óptimo de Eucalyptus nitens en Galicia introduciendo la fiscalidad en el análisis. XII Congreso de Economía Agraria.

Ayuga-Téllez, E., García-Iruela, A., Rielo, J.C., González-García, C., 2022. Actions for Monitoring the Gonipterus Pest in Eucalyptus on the Cantabrian Coast. Agronomy (Basel) 12, 1692. https://doi.org/10.3390/agronomy12071692.

Barrio-Anta, M., Castedo-Dorado, F., Cámara-Obregón, A., López-Sánchez, C.A., 2021. Integrating species distribution models at forest planning level to develop indicators for fast-growing plantations. A case study of Eucalyptus globulus Labill. in Galicia (NW Spain). For. Ecol. Manag. 491, 119200 https://doi.org/10.1016/j.foreco.2021.119200.

BASOA foundation, 2017. Distinción entre especies de Eucalipto. <https://basoa.org/es/comunicacion/noticias/2881-distincion-entre-especies-de-eucalipto> (Accessed 12 July 2023).

Battaglia, M., Beadle, C., Loughhead, S., 1996. Photosynthetic temperature responses of Eucalyptus globulus and Eucalyptus nitens. Tree Physiol. 16(1_2) https://doi.org/10.1093/treephys/16.1-2.81, 81–89. PMID: 14871750.

Bayly, M.J., 2016. Phylogenetic studies of eucalypts: fossils, morphology and genomes. Proc. R. Soc. Vic. 128, 12–24. https://doi.org/10.1071/rs16002.

Beadle, C.L., Banham, P., Worledge, D., Russell, S.L., 2001. Effect of irrigation on growth and fibre quality of Eucalyptus globulus and Eucalyptus nitens. Appita J. 54, 144–147.

Brus, D.J., Nabuurs, G.J., Hengeveld, G.M., Walvoort, D.J.J., Goedhart, P.W., Heidema, A.H., Gunia, K., 2011. Tree Species Maps for European Forests. European Forest Institute.

Calviño-Cancela, M., Rubido-Bará, M., 2013, Invasive potential of *Eucalyptus globulus*: Seed dispersal, seedling recruitment and survival in habitats surrounding plantations, Forest Ecology and Management, 305, 129-137, <https://doi.org/10.1016/j.foreco.2013.05.037>.

Calviño-Cancela, M., van Etten, E.J., 2018. Invasive potential of Eucalyptus globulus and Pinus radiata into native eucalypt forests in Western Australia. For. Ecol. Manag. 424, 246–258.

Chen, Y., Peng, Z., Ye, Y., Jiang, X., Lu, D., Chen, E., 2021. Exploring a uniform procedure to map Eucalyptus plantations based on fused medium–high spatial resolution satellite images. Int. J. Appl. Earth Observ. Geoinform. 103, 102462 https://doi.org/10.1016/j.jag.2021.102462.

Close, D.C., Beadle, C.L., Brown, P.H., Holz, G.K., 2000. Cold-induced photoinhibition affects establishment of Eucalyptus nitens (deane and maiden) maiden and Eucalyptus globulus Labill. Trees - Struct. Funct. 15, 32–41.

Coppen, J.J.W. (Ed.)., 2002. Eucalyptus. CRC Press. <https://doi.org/10.1201/9780203219430>.

da Costa, L.B., de Carvalho, O.L.F., de Albuquerque, A.O., Gomes, R.A.T., Guimarães, R. F., de Carvalho Júnior, O.A., 2022. Deep semantic segmentation for detecting eucalyptus planted forests in the Brazilian territory using sentinel-2 imagery. Geocarto int. 37, 6538–6550. https://doi.org/10.1080/10106049.2021.1943009.

Dalponte, M., Oerka, H.O., 2021. varSel: sequential forward floating selection using jeffries-matusita distance. R Package Vers. 2. https://CRAN.R-project.org/package=varSel.

Datt, B., 1999. Remote sensing of foliar biochemistry and biophysical properties in Eucalyptus species: application of high spectral resolution reflectance measurements. School of Geography, The University of New South Wales, Sydney. PhD Thesis.

Davidson, N.J., Battaglia, M., Close, D.C., 2004. Photosynthetic responses to overnight frost in Eucalyptus nitens and E. globulus. Trees - Struct. Funct. 18, 245–252.

Deflorio, G., Barry, K.M., Johnson, C., Mohammed, C.L., 2007. The influence of wound location on decay extent in plantation-grown Eucalyptus globulus and Eucalyptus nitens. For. Ecol. Manag. 242, 353–362.

Deng, X., Guo, S., Sun, L., Chen, J., 2020. Identification of short-rotation eucalyptus plantation at large scale using multi-satellite imageries and cloud computing platform. Remote sens. 12, 2153. https://doi.org/10.3390/rs12132153.

Dog, 2021. ORDEN de 9 de febrero de 2021 por la que se modifica el anexo I de la Orden de 19 de mayo de 2014 por la que se establecen los modelos silvícolas o de gestión forestal orientativos y referentes de buenas prácticas forestales para los distritos forestales de Galicia. DOG. 39, 12222.

Domingues, R.M.A., Sousa, G.D.A., Silva, C.M., Freire, C.S.R., Silvestre, A.J.D., Neto, C. P., 2011. High value triterpenic compounds from the outer barks of several Eucalyptus species cultivated in Brazil and in Portugal. Ind. Crops Prod. 33, 158–164. https://doi.org/10.1016/j.indcrop.2010.10.006.

Downes, G., Beadle, C., Worledge, D., 1999. Daily stem growth patterns in irrigated Eucalyptus globulus and E. nitens in relation to climate. Trees 14, 102–111. https://doi.org/10.1007/PL00009752.

ESA (European Space Agency), 2015. ESA Standard Document—Sentinel-2 User Handbook. 2015. <https://sentinels.copernicus.eu/web/sentinel/user-guides/document-library/-/asset_publisher/xlslt4309D5h/content/sentinel-2-user-handbook> (Accessed on 20 December 2022).

ESA (European Space Agency), n.d. Copernicus and European Comission. Copernicus Open Access Hub. (Accessed on 16 February 2022).

ESA (European Space Agency), n.d.b. Sentinel Online. Processing levels. <https://sentinels.copernicus.eu/web/sentinel/user-guides/sentinel-2-msi/processing-levels> (Accessed on 12 December 2023).

Fassnacht, F.E., Latifi, H., Stereńczak, K., Modzelewska, A., Lefsky, M., Waser, L.T., Straub, C., Ghosh, A., 2016. Review of studies on tree species classification from remotely sensed data. Rem. Sens. Environ. 186, 64–87. https://doi.org/10.1016/j.rse.2016.08.013.

Feng, Q., Liu, J., Gong, J., 2015. UAV remote sensing for urban vegetation mapping using random forest and texture analysis. Rem. Sens. 7, 1074–1094. https://doi.org/10.3390/rs70101074.

Forstmaier, A., Shekhar, A., Chen, J., 2020. Mapping of eucalyptus in natura 2000 areas using sentinel 2 imagery and artificial neural networks. Remote Sens. 12 (14), 2176. https://doi.org/10.3390/rs12142176.

Forsyth, G.G., Richardson, D.M., Brown, P.J., Van Wilgen, B.W., 2004. A rapid assessment of the invasive status of Eucalyptus species in two South African provinces. S. Afr. J. Sci. 100, 75–77.

Franklin, S.E., Ahmed, O.S., 2018. Deciduous tree species classification using object-based analysis and machine learning with unmanned aerial vehicle multispectral data. Int. J. Rem. Sens. 39 (15–16), 5236–5245. https://doi.org/10.1080/01431161.2017.1363442.

Gao, B.C., 1996. NDWI - a normalized difference water index for remote sensing of vegetation liquid water from space. Rem. Sens. Environ. 58, 257–266. https://doi.org/10.1016/S0034-4257(96)00067-3.

Gonçalves, C.I., Vilas-Boas, L., Branco, M., Rezende, G.D., Valente, C., 2019. Host susceptibility to Gonipterus platensis (Coleoptera: Curculionidae) of Eucalyptus species. Ann. For. Sci 76, 63.

González-Gómez, M., Otero Giráldez, M.S., Álvarez-Díaz, M., 2011. Explaining wood stock increases in times of decreasing profitability: a statistical analysis. For. Policy Econ. 13, 176–183. https://doi.org/10.1016/j.forpol.2010.11.008.

Gutiérrez, L.,1976. Atlas del Eucalipto: tomo I-información y ecología. Ministerio de Agricultura. Instituto Nacional de Investigaciones Agrarias. Instituto Nacional para la Conservación de la Naturaleza. <http://libros.inia.es/libros/product_info.php?cPath=5&products_id=319> (Accessed on 12 December 2022).

Harwood, C., 2011. Introductions: doing it right. En Walker J. (Ed.). Developing a Eucalypt Resource. Learning from Australia and Elsewhere, 43-54. Wood Technology Research Centre, University of Canterbury, New Zealand.

ICNF (Instituto da Instituto da Conservação da Natureza e das Florestas), 2015. 6.° Inventário Florestal Nacional. Relatório final. <https://www.icnf.pt/api/file/doc/c8cc40b3b7ec8541> (Accessed 12 December 2022).

Immitzer, M., Neuwirth, M., Böck, S., Brenner, H., Vuolo, F., Atzberger, C., 2019. Optimal input features for tree species classification in central europe based on multi-temporal sentinel-2 data. Remote Sens. 11, 2599. https://doi.org/10.3390/rs11222599.

Kibblewhite, R.P., Johnson, B.I., Shelbourne, C.J.A., 2000. Kraft pulp qualities of Eucalyptus Nitens, E. Globulus, E. maidenii, at ages 8 and 11 years. N. Z. J. For. Sci. 30, 447–457.

Kogan, F.N., 1995. Droughts of the late 1980s in the United States as derived from NOAA polar-orbiting satellite data. Bull. Am. Meteorol. Soc. 76 (5), 655–668. https://doi.org/10.1175/1520-0477(1995)076<0655:DOTLIT>2.0.CO;2.

Kumar, L., 2007. A comparison of reflectance characteristics of some Australian eucalyptus species based on high spectral resolution data — discriminating using the visible and NIR regions. J. Spat. Sci. 51–64 https://doi.org/10.1080/14498596.2007.9635122.

Lewiński, S., Nowakowski, A., Malinowski, R., Rybicki, M., Kukawska, E., Krupiński, M., 2017. Aggregation of Sentinel-2 time series classifications as a solution for multitemporal analysis. Image and Signal Processing for Remote Sensing XXIII SPIE 10427, 13. https://doi.org/10.1117/12.2277976.

López, G., 2002. Guía de los árboles y arbustos de la Península Ibérica y, Baleares. ed. Mundi-Prensa, Madrid.

Messier, C., Bauhus, J., Sousa-Silva, R., Auge, H., Baeten, L., Barsoum, N., Bruelheide, H., Caldwell, B., Cavender-Bares, J., Dhiedt, E., Eisenhauer, N., Ganade, G., Gravel, D., Guillemot, J., Hall, J.S., Hector, A., Hérault, B., Jactel, H., Koricheva, J., Kreft, H., Mereu, S., Muys, B., Nock, C.A., Paquette, A., Parker, J.D., Perring, M.P., Ponette, Q., Potvin, C., Reich, P.B., Scherer-Lorenzen, M., Schnabel, F., Verheyen, K., Weih, M., Wollni, M., Zemp, D.C., 2021. For the sake of resilience and multifunctionality, let's diversify planted forests! Conserv. Let. 15, e12829.

Misra, G., Cawkwell, F., Wingler, A., 2020. Status of Phenological Research Using Sentinel-2 Data: A Review, 2020. Remote Sens., 12, 2760. <https://doi.org/10.3390/rs12172760>.

MITECO, 2011a. Cuarto Inventario Forestal Nacional, Galicia. Dirección General de Medio Natural y Política Forestal Ministerio de Medio Ambiente, y Medio Rural y Marino. ISBN: 978-84-8014-813-9.

MITECO, 2011b. Mapa Forestal de España (MFE) de máxima actualidad. <https://www.miteco.gob.es/es/cartografia-y-sig/ide/descargas/biodiversidad/mfe.aspx> (Accessed 11 January 2022).

MITECO, 2017. Solicitud de dictamen sobre la posible inclusión de Eucalyptus camaldulensis, E. globulus, E. nitens y cualquier otra especie del género Eucalyptus en el Catálogo Español de Especies Exóticas Invasoras regulado por el R.D. 630/2013, de 2 de agosto y remitida al MAPAMA por el alcalde del Ayuntamiento de Teo (A Coruña). MITECO.

Moncur, M.W., Hasan, O., 1994. Floral induction in *Eucalyptus nitens*. Tree Physiol. 14 (11), 1303–1312. https://doi.org/10.1093/treephys/14.11.1303.

Neilan, J., Thompson, D., 2008. Eucalyptus as a potential biomass species for Ireland. COFORD Connect. Reprod. Mater. 15.

Ngugi, M.R., Doley, D., Cant, M., Botkin, D.B., 2015. Growth rates of Eucalyptus and other Australian native tree species derived from seven decades of growth monitoring. J. For. Res. 26, 811–826. https://doi.org/10.1007/s11676-015-0095-z.

Novo-Gomez, A., Gonzalez-Jorge, H., Comesaña-Cebral, L., Lorenzo-Cimadevilla, H., Martinez-Sanchez, J., 2022. Semi-automated tree species classification based on roughness parameters using airborne lidar data. DYNA 97 (5), 528–534. https://doi.org/10.6036/10567.

Oliveira, D., Martins, L., Mora, A., Damásio, C., Caetano, M., Fonseca, J., Ribeiro, R.A., 2021. Data fusion approach for eucalyptus trees identification. Int. J. Remote Sens. 42, 4087–4109. https://doi.org/10.1080/01431161.2021.1883198.

Orwa, C., Mutua, A., Kindt, R., Jamnadass, R., Simons, A., 2009. Agroforestree Database: a tree reference and selection guide version 4.0. <http://www.worldagroforestry.org/af/treedb/> (Accessed 12 December 2022).

Peerbhay, K.Y., Mutanga, O., Ismail, R., 2013. Commercial tree species discrimination using airborne AISA Eagle hyperspectral imagery and partial least squares discriminant analysis (PLS-DA) in KwaZulu–Natal, South Africa. ISPRS J. Photogramm. Remote Sens. 79, 19–28. https://doi.org/10.1016/j.isprsjprs.2013.01.013.

Peerbhay, K.Y., Mutanga, O., Ismail, R., 2014. Investigating the capability of few strategically placed worldview-2 multispectral bands to discriminate forest species in KwaZulu-Natal, South Africa. IEEE J. Select. Top. Appl. Earth Observ. Rem. Sens. 7, 307–316. https://doi.org/10.1109/JSTARS.2013.2262634.

Pérez, S., Renedo, C.J., Ortiz, A., Mañana, M., Silió, D., 2006. Energy evaluation of the Eucalyptus globulus and the Eucalyptus nitens in the north of Spain (Cantabria). Thermochim. Acta 451, 57–64.

Pérez-Cruzado, C., Merino, A., Rodríguez-Soalleiro, R., 2011. A management tool for estimating bioenergy production and carbon sequestration in Eucalyptus globulus and Eucalyptus nitens grown as short rotation woody crops in north-west Spain. Biomass Bioenergy 35, 2839–2851. https://doi.org/10.1016/j.biombioe.2011.03.020.

Pérez-Cruzado, C., Rodríguez-Soalleiro, R., 2011. Improvement in accuracy of aboveground biomass estimation in Eucalyptus nitens plantations: effect of bole sampling intensity and explanatory variables. Forest Ecol. Manage. 261, 2016–2028. https://doi.org/10.1016/j.foreco.2011.02.028.

Persson, M., Lindberg, E., Reese, H., 2018. Tree species classification with multi-temporal sentinel-2 data. Remote Sens. 10, 1794. https://doi.org/10.3390/rs10111794.

Pinheiro Ferreira, M., Hubert Wagner, F., Luiz, E.O.C.A., Edemir Shimabukuro, Y., de Souza Filho, C.R., 2019. Tree species classification in tropical forests using visible to shortwave infrared WorldView-3 images and texture analysis. ISPRS J. Photogram. Rem. Sens. 149, 119–131. https://doi.org/10.1016/j.isprsjprs.2019.01.019.

Pinkard, E.A., 2002. Effects of pattern and severity of pruning on growth and branch development of pre-canopy closure Eucalyptus nitens. For. Ecol. Manag. 157, 217–230. https://doi.org/10.1016/S0378-1127(00)00647-2.

Pretzsch, H., 2008. Description and Analysis of Stand Structures. Springer, Berlin Heidelberg, 279–280. 10.1007/978-3-540-88307-4.

Qiao, H., Wu, M., Shakir, M., Wang, L., Kang, J., Niu, Z., 2016. Classification of small-scale eucalyptus plantations based on NDVI time series obtained from multiple high-resolution datasets. Remote Sens. 8, 117. https://doi.org/10.3390/rs8020117.

Ramachandran, P., Zoph, B., Le, Q. V., 2017. Searching for Activation Functions arXiv, 1–13. http://arxiv.org/abs/1710.05941.

Ramnath, L., Sithole, B., Govinden, R., 2018. The effects of wood storage on the chemical composition and indigenous microflora of eucalyptus species used in the pulping industry. BioRes 13, 86–103. https://doi.org/10.15376/biores.13.1.86-103.

Rapidlasso, G., 2023. LAStools – efficient tools for LIDAR processing. <http://www.cs.unc.edu/~isenburg/lastools/>. (Accessed 13 March 2023).

Rodríguez-Rajo, F.J., Aira, M.J., Fernández-González, M., Seijo, C., Jato, V., 2011. Recent trends in airborne polen for tree species in Galicia, NW Spain. Clim. Res. 48, 281–291. https://doi.org/10.3354/cr00966.

Roussel, J.-R., Auty, D., Coops, N.C., Tompalski, P., Goodbody, T.R.H., Meador, A.S., Bourdon, J.-F., de Boissieu, F., Achim, A., 2020. lidR: an R package for analysis of Airborne Laser Scanning (ALS) data. Remote Sens. Environ. 251, 112061 https://doi.org/10.1016/j.rse.2020.112061.

Santopuoli, G., Temperli, C., Alberdi, I., Barbeito, I., Bosela, M., Bottero, A., Klopčič, M., Lesinski, J., Panzacchi, P., Tognetti, R., 2021. Pan-European sustainable forest management indicators for assessing Climate-Smart Forestry in Europe. Can. J. For. Res. 51, 1741–1750. https://doi.org/10.1139/cjfr-2020-0166.

Sen, R., Goswami, S., Chakraborty, B., 2019. Jeffries-Matusita distance as a tool for feature selection. In: 2019 International Conference on Data Science and Egineering (ICDSE). https://doi.org/10.1109/ICDSE47409.2019.8971800.

Seng Hua, L., Wei Chen, L., Antov, P., Kristak, L., Md Tahir, P., 2022. Engineering wood products from eucalyptus spp. Adv. Mater. Sci. Eng. 2022, 1–14. https://doi.org/10.1155/2022/8000780.

Sentinelhub, 2023a. Normalized Difference Moisture Index (NDMI). <https://custom-scripts.sentinel-hub.com/custom-scripts/sentinel-2/ndmi/> (Accessed 22 June 2023).

Sentinelhub, 2023b. Sentinel-2 RS indices. <https://custom-scripts.sentinel-hub.com/custom-scripts/sentinel-2/indexdb/> (Accessed 22 June 2023).

Shahi, K., Shafri, H.Z.M., Taherzadeh, E., 2014. A novel spectral index for automatic shadow detection in urban mapping based on worldview-2 satellite imagery. Zenodo. https://doi.org/10.5281/ZENODO.1096194.

Shang, X., Chisholm, L.A., 2014. Classification of Australian native forest species using hyperspectral remote sensing and machine-learning classification algorithms. IEEE J. Sel. Top. Appl. Earth Observ. Rem. Sens. 7, 2481–2489. https://doi.org/10.1109/JSTARS.2013.2282166.

Shannon, C.E., 1948. A mathematical theory of communication. Bell System Tech. J. 27 (379–423), 623–656.

Sibanda, M., Buthelezi, S., Ndlovu, H.S., Mothapo, M.C., Mutanga, O., 2021. Mapping the Eucalyptus spp woodlots in communal areas of Southern Africa using Sentinel-2 Multi-Spectral Imager data for hydrological applications. Phys. Chem. Earth., Parts A/B/C 122, 102999. https://doi.org/10.1016/j.pce.2021.102999.

Smith, A.H., Gill, W.M., Pinkard, E.A., Mohammed, C.L., 2007. Anatomical and histochemical defence responses induced in juvenile leaves of Eucalyptus globulus and Eucalyptus nitens by Mycosphaerella infection. For. Pathol. 37, 361–373.

Tarpley, J.D., Schneider, R.L., Money, R.L., 1984. Global vegetation indices from the NOAA-7 meteorological satellite. J. Clim. Appl. Meteorol. 23 (1984), 491–494. https://doi.org/10.1175/1520-0450(1984)023<0491:GVIFTN>2.0.CO;2.

Team, K., 2022. Keras documentation: About keras. <https://keras.io/about/> (Accessed 12 December 2022).

Tolosana, E., Diaz-Balteiro, L., Lobo-Huici, E., 2017. Estudio del turno óptimo de Eucalyptus globulus en el norte de España. VII Congreso Forestal Español. ISBN 978-84-941695-2-6.

Tomé, M., Almeida, M.H., Barreiro, S., Branco, M.R., Deus, E., Pinto, G., Silva, J.S., Soares, P., Rodríguez-Soalleiro, R., 2021. Opportunities and challenges of Eucalyptus plantations in Europe: the Iberian Peninsula experience. Eur. J. For. Res. 140, 489–510. https://doi.org/10.1007/s10342-021-01358-z.

Toulemont, A., Olivier, M., Clerc, S., Bellouard, R., Reina, F., Gascon, F., Luce, J.F., Mavrocordatos, C., Boccia, V., Neeck, S.P., Kimura, T., Babu, S.R., Hélière, A., 2021. Copernicus Sentinel-2C/D Multi Spectral Instrument full field of view spectral characterization. Proc. of SPIE 11858, Sensors, Systems, and Next-Generation Satellites XXV, 118580V. <https://doi.org/10.1117/12.2593729>.

Van Rossum, G., Drake Jr, F.L., 1995. Python tutorial. Centrum voor Wiskunde en Informatica, Amsterdam, The Netherlands.

Verma, N.K., Lamb, D.W., Sinha, P., 2019. Airborne LiDAR and high resolution multispectral data integration in Eucalyptus Tree species mapping in an Australian farmscape. Geocarto Int. 37, 70–90. https://doi.org/10.1080/10106049.2019.1700555.

Watt, M.S., Rubilar, R., Kimberley, M.O., Kriticos, D.J., Emhart, V., Mardones, O., Acevedo, M., Pincheira, M., Stape, J., Fox, T., 2014. Using seasonal measurements to inform ecophysiology: extracting cardinal growth temperatures for process-based growth models of five Eucalyptus species/crosses from simple field trials. New Zeland J. Forest. Sci. 44, 9. https://doi.org/10.1186/s40490-014-0009-4.

Wiseman, D., Pinkard, E., Wardlaw, T., Mohammed, C., Hall, M., Beadle, C., 2009. Growth responses of Eucalyptus globulus and E. nitens to pruning and fertiliser treatments in a plantation managed for solid-wood products. South. For. 71, 21–29.

Wu, Y., Li, J., Kong, Y., Fu, Y., 2016. Deep convolutional neural network with independent softmax for large scale face recognition. In: Proceedings of the 24th ACM international conference on Multimedia, 1063-1067. <https://doi.org/10.1145/2964284.2984060>.

Wu, Y., Zhang, X., 2020. Object-based tree species classification using airborne hyperspectral images and LiDAR data. Forests 11, 32. https://doi.org/10.3390/f11010032.

Xiao, C., Li., P., Feng, Z., Liu, Y., Zhang, X., 2020. Sentinel-2 red-edge spectral indices (RESI) suitability for mapping rubber boom in Luang Namtha Province, northern Lao PDR. Int. J. Appl Earth Obs Geoinf. 93, 102176. <https://doi.org/10.1016/j.jag.2020.102176>.

Xunta de Galicia, 2023. Observatorio forestal. <https://ovmediorural.xunta.gal/es/consultas-publicas/observatorio-forestal> (Accessed 13 March 2023).

Yadav, B.K.V., Lucieer, A., Baker, S.C., Jordan, G.J., 2021. Tree crown segmentation and species classification in a wet eucalypt forest from airborne hyperspectral and LiDAR data. Int. J. Remote Sens. 42, 7952–7977. https://doi.org/10.1080/01431161.2021.1956699.